

# A B cell-IgA-epithelial axis enhances antitumor immunity and improves outcome in HPV-associated penile squamous cell carcinoma

Received: 18 March 2024

Accepted: 27 November 2025

Published online: 11 December 2025

 Check for updates

Tao Tao<sup>1,3</sup>, Lianbang Zhu<sup>2,3</sup>, Deyun Shen<sup>1,3</sup>, Jiayang Zhang<sup>2</sup>, Panrui Zhang<sup>2</sup>, Zhixi Gu<sup>2</sup>, Dan Cao<sup>2</sup>, Jun Xiao<sup>1</sup>✉ & Wen Pan<sup>2</sup>✉

Penile squamous cell carcinoma (PSCC) is a rare, aggressive malignancy, with HPV driving approximately 50% of cases and correlating with improved outcomes. In this study, we perform single-cell RNA sequencing on tumor microenvironment (TME) cells from 23 treatment-naive PSCC patients, including 11 cases reported previously, and validate our findings in a larger cohort of 85 patients. Our analysis reveals significant immune cell infiltration in PSCC, with HPV<sup>+</sup> tumors exhibiting elevated levels of tumor-infiltrating B cells, plasma cells, tertiary lymphoid structures, and IgA secretion. A subset of malignant epithelial cells in HPV<sup>+</sup> PSCC express the polymeric IgA receptor (PIGR), facilitating IgA transcytosis and inducing anti-tumor responses. Functional studies show that PIGR overexpression promotes tumor apoptosis and enhances immune responses, with these effects diminish in IgA-deficient mice. Elevated IgA and PIGR expression correlate with improved survival. These findings provide a single-cell atlas of the PSCC TME, highlighting the B cell–IgA–PIGR axis as a pivotal driver of antitumor immunity and clinical outcomes in HPV<sup>+</sup> PSCC.

Penile cancer is a rare urologic carcinoma with orphan disease designation and a prevalence of 0.1–1 per 100,000 men in high-income countries<sup>1</sup>. However, the incidence is higher up to 10% among male malignancies in the developing countries of African, Asian and South American<sup>2</sup>. There are various risk factors that cause the different incidence in global regions, including the absence of protective circumcision, chronic inflammatory conditions and HPV infection<sup>3,4</sup>. The majority of penile cancers originate from the squamous cells and are collectively termed penile squamous cell carcinomas (PSCC), with only about half of patients surviving beyond 5 years<sup>1,5</sup>. Although rare, PSCC

is closely linked to HPV infection, with a pooled HPV prevalence of 50.8%<sup>4,6,7</sup>. Clinically, PSCC can be divided into HPV-driven and non-HPV-related subtypes<sup>8</sup>. HPV exerts its oncogenic influence through the viral oncoproteins E6 and E7, which disrupt cell cycle regulation and promote genomic instability<sup>9,10</sup>. Despite these oncogenic mechanisms, HPV<sup>+</sup> PSCC is associated with better outcomes compared to HPV cases<sup>11–13</sup>. The reasons for this paradox, however, remain limited.

To date, multi-omics approaches have shed light on the genomic, epigenetic, and transcriptomic landscape of PSCC, revealing somatic mutations<sup>14–17</sup>, genome-wide methylation patterns, and gene

<sup>1</sup>Department of Urology, The First Affiliated Hospital of USTC, Centre for Leading Medicine and Advanced Technologies of IHM, Division of Life Sciences and Medicine, University of Science and Technology of China, Hefei, China. <sup>2</sup>Key Laboratory of Immune Response and Immunotherapy, Center for Advanced Interdisciplinary Science and Biomedicine of IHM, School of Basic Medical Sciences, Division of Life Sciences and Medicine, University of Science and Technology of China, Hefei, China. <sup>3</sup>These authors contributed equally: Tao Tao, Lianbang Zhu, Deyun Shen. ✉e-mail: [ixiaojun@ustc.edu.cn](mailto:ixiaojun@ustc.edu.cn); [wenpan@ustc.edu.cn](mailto:wenpan@ustc.edu.cn)

expression profiles<sup>18</sup> in PSCC. Recent whole-exome sequencing in PSCC has shown that HPV PSCC tends to be associated with TP53 loss-of-function mutation<sup>16</sup>. Another work described the single-cell composition of the PSCC TME and unveiled TP53 mutations as a driver of an aggressive phenotype, irrespective of HPV status<sup>19</sup>. While these studies have focused on tumor-intrinsic factors, the influence of the immune microenvironment, particularly in HPV<sup>+</sup> PSCC, remains unclear.

HPV infection creates a distinct inflammatory immune environment, which may reshape the cellular composition and functional dynamics within the PSCC TME. Given the rarity of PSCC and the limited availability of clinical samples, a detailed characterization of the TME, specifically comparing HPV<sup>+</sup> and HPV<sup>-</sup> PSCC, is essential.

Such insights could help clarify the differential outcomes between these two groups<sup>20</sup>. Furthermore, the validation of these findings across larger PSCC cohorts is needed to ensure robustness and clinical relevance.

In this study, we apply scRNA-seq to explore the heterogeneity and differences of the TME in HPV<sup>+</sup> versus HPV<sup>-</sup> PSCC. We aim to identify key immune cell populations and their roles within the TME. We employ a range of validation techniques, including immunohistochemistry (IHC), multiplex immunofluorescence (mIF), flow cytometry (FCM) and enzyme-linked immunosorbent assay (ELISA) to investigate the immune cell composition and immunoglobulin (Ig) production across a larger PSCC cohort. Our study also explores the heterogeneity of malignant epithelial cells, focusing on a subset expressing the polymeric IgA receptor (PIGR). Using PIGR-overexpressing PSCC primary cells and in vivo xenograft models, we investigate the roles of an immune-PIGR axis in mediating anti-tumor effects.

## Results

### Single-cell RNA-seq profiling of PSCC

To explore the complexity and heterogeneity of the tumor microenvironment (TME) in PSCC, we performed scRNA-seq on 23 tumor specimens and 6 paired normal adjacent tissues (NATs) from patients as the discovery cohort, including 11 cases reported in our previously published work<sup>20</sup> (Fig. 1A, Supplementary Fig. 1A and Supplementary Table 1). One NAT sample (P4N) failed library quality control, leaving 28 high-quality samples (23 tumors and 5 NATs) for downstream analysis. HPV status for the discovery cohort was assessed using p16 immunohistochemistry (IHC)<sup>19,21</sup>, HPV16/18 DNA in situ hybridization, and HPV PCR (Supplementary Fig. 1B–D). In addition, we collected a larger cohort of PSCC cases to support validation using orthogonal assays (see “Methods”), with detailed clinical and pathological information, as well as sample allocation and time-sequential accrual (Supplementary Fig. 1A and Supplementary Table 2, 3).

Among the 28 samples analyzed by single-cell RNA sequencing, a total of 12.3 billion mapped reads were generated, with 29,845 genes detected (unique molecular identifiers (UMIs) > 0). On average, each sample produced over 441 million sequencing reads with an average sequencing saturation (covering the fraction of library complexity) of 63.2% (Supplementary Table 4). A total of 202,424 single cells passed quality control filters (based on gene expression and mitochondrial genes ratios; see “Methods”) (Supplementary Fig. 2A). On average, each cell had 2209 detected genes and 7138 UMIs, indicating sufficient transcriptome coverage and a representative capture of expressed genes (Supplementary Table 5).

### Single-cell landscape of the tumor microenvironment in PSCC

We next used Seurat<sup>22</sup> R package for unsupervised clustering and the Uniform Manifold Approximation and Projection (UMAP) for dimensionality reduction and cell visualization (see Methods). We analyzed the total 202,424 cells from the discovery cohort, which captures the full diversity of TME cells, including both immune and non-immune

populations, across tumor and NAT samples. All cells expressed high levels of housekeeping genes, such as *ACTB*, *B2M* and *GAPDH* (Supplementary Fig. 2B) and were then grouped into 17 distinct clusters using unsupervised Louvain clustering. Based on known cell markers, we classified 17 clusters into four major cell types: immune cells (*PTPRC*), epithelial cells (*KRT5*), endothelial cells (*VWF*), and cancer-associated fibroblasts (CAFs) (*COL6A2*) (Fig. 1B, C, Supplementary Fig. 2C). These cell types were consistently identified across PSCC patients, though their relative proportions varied, likely due to patient-specific factors, inherent sampling variability, etc (Fig. 1D). Among them, the identified immune cells emerged as the predominant population within tumor tissues, indicating significant immune infiltration in PSCC (Fig. 1E). Consistent the results from scRNA-seq analysis, mIF confirmed the distribution of immune cells (CD45), epithelial cells (*KRT5*), endothelial cells (CD31), and CAFs (VIM) across NATs and tumor tissues in PSCC (Fig. 1F).

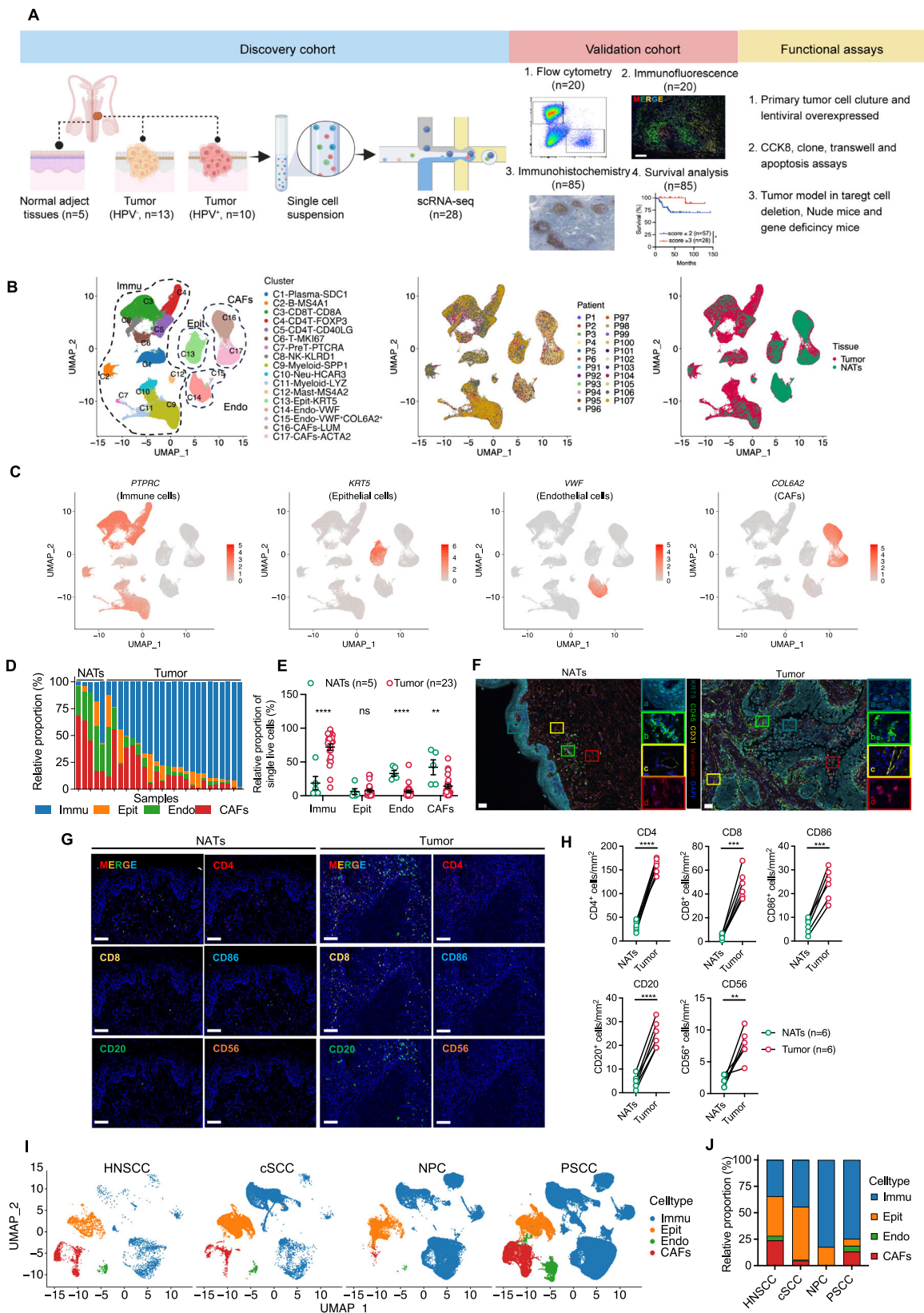
To validate our scRNA-seq findings, we performed mIF staining on the same PSCC samples, targeting five immune subpopulations, including CD4 and CD8 for TIL-Ts, CD20 for TIL-Bs, CD86 for antigen-presenting cells (APC, macrophages and dendritic cell), and CD56 for NK (Fig. 1G and Supplementary Table 3). In comparison to NATs, the absolute numbers of CD4<sup>+</sup>, CD8<sup>+</sup>, CD20<sup>+</sup>, CD86<sup>+</sup>, and CD56<sup>+</sup> cells per tissue area were significantly increased in tumor tissues (Fig. 1H). These results support our conclusion that PSCC tumors exhibit enhanced immune cell infiltration compared to NATs.

To contextualize our findings, we compared our PSCC data with publicly available datasets from other squamous cell carcinomas (SCCs), including head and neck squamous cell carcinoma (HNSCC)<sup>23</sup>, nasopharyngeal carcinoma (NPC)<sup>24</sup> and cutaneous squamous cell carcinoma (cSCC)<sup>25</sup>. Similarly, immune (*PTPRC*), epithelial (*KRT5*), endothelial (*PECAMI*) and CAFs (*COL6A2*) were identified using established markers in each dataset (Supplementary Fig. 2D). While the four cell types were present in all squamous cell malignancies examined, the relative proportions varied across different SCC types (Fig. 1I). Notably, both PSCC and NPC exhibited higher immune cell infiltration, with PSCC showing a dominant immune cell compartment (74.62%) within TME (Fig. 1J).

### Distinctive TIL-Bs composition in HPV<sup>+</sup> vs. HPV<sup>-</sup> PSCC

To explore the differences of tumor infiltrating immune cells between HPV<sup>-</sup> and HPV<sup>+</sup> PSCC, we focus on 12 immune clusters from 23 PSCC patients, including 87,790 cells from HPV<sup>-</sup> tumor and 46,994 cells from HPV<sup>+</sup> tumor (Fig. 2A). The remaining immune cell subpopulations were categorized into tumor-infiltrating B cells (TIL-Bs), tumor-infiltrating T cells (TIL-Ts), natural killer (NK) cells, and myeloid-derived cells (Fig. 2A). Among the immune cell populations, we identified two major TIL-Bs populations: SDC1<sup>+</sup> plasma cells (C1-Plasma-SDC1) and CD20<sup>+</sup> B cells (C2-B-MS4A1). TIL-Ts were subdivided into five clusters (C3–C7), including CD8<sup>+</sup> TIL-Ts (C3-CD8T-CD8A), two subtypes of CD4<sup>+</sup> TIL-Ts cells (C4-CD4T-FOXP3 and C5-CD4T-CD40LG), a proliferative TIL-Ts cluster (C6-T-MKI67), and early T-cell precursors (C7-PreT-PTCRA). Myeloid-derived cells were grouped into four clusters, including C9-Myeloid-SPP1, neutrophils (C10-Neu-HCAR3), C11-Myeloid-LYZ and mast cells (C12-Mast-MS4A2) (Fig. 2A). For 12 clusters, we found that SDC1<sup>+</sup> plasma cells (C1) and CD20<sup>+</sup> B cells (C2) were increased in HPV<sup>+</sup> PSCC, while cluster 6 was enriched in HPV<sup>-</sup> PSCC (Fig. 2B, C). Among four immune cell subpopulations, TIL-Bs also emerged as a significant increase in HPV<sup>+</sup> compared to HPV<sup>-</sup> tumor (Fig. 2D). Interestingly, this enrichment of TIL-Bs has also been observed in other HPV-associated cancers, such as HPV<sup>+</sup> HNSCC<sup>26–28</sup> and HPV<sup>+</sup> oropharyngeal squamous cell carcinoma (OPC)<sup>29</sup>, suggesting a common feature of HPV-associated squamous cell carcinoma.

To validate our scRNA-seq findings, we performed FCM analysis on CD45<sup>+</sup> immune cells isolated from available fresh tumor tissues of 9 HPV<sup>+</sup> and 11 HPV<sup>-</sup> PSCC patients (Fig. 2E, Supplementary Fig. 1A and



Supplementary Table 3). The results demonstrated a significant increase in the proportion of TIL-Bs within the total CD45<sup>+</sup> immune cells in HPV<sup>+</sup> PSCC compared to HPV<sup>-</sup> PSCC (Fig. 2F). In contrast, the proportions of total CD45<sup>+</sup> immune cells, CD3<sup>+</sup> TIL-Ts, CD4<sup>+</sup> TIL-Ts and CD8<sup>+</sup> TIL-Ts showed no significant differences between the two groups (Fig. 2F). We further validated these findings through double-plex IHC

staining for B cells (CD20) and T cells (CD3) in tumor sections from our validation cohort of 85 PSCC patients (33 HPV<sup>+</sup> and 52 HPV<sup>-</sup> cases) (Supplementary Fig. 1A and Supplementary Table 3). Importantly, the clinical outcomes observed in our validation cohort were consistent with previous studies, showing that HPV<sup>+</sup> PSCC patients generally have better survival than HPV<sup>-</sup> patients<sup>11-13</sup> (Fig. 2G). This consistency in

**Fig. 1 | Single-cell landscape of the tumor microenvironment in PSCC.**

**A** Schematic overview of the experimental strategy (Created in BioRender). Pan, W. (2025) <https://biorender.com/udc23v6>. Surgical tumor specimens and paired normal adjacent tissues (NATs) were collected from 23 treatment-naïve PSCC patients (Tumor,  $n = 23$ ; NATs,  $n = 5$ ) and processed for single-cell RNA sequencing and transcriptomic analysis. **B** UMAP plot of 202,424 cells from the discovery cohort, showing cell components in PSCC, color-coded by cell type (left), patients (middle) and tissue (right). **C** Normalized expression of marker genes used to define four major cell types as shown in **(B)**. **D** Relative abundance of four major cell types in tumor tissues ( $n = 23$ ) or NATs ( $n = 5$ ) from each PSCC patient, excluding PN4. **E** Bar graph comparing the relative proportions of the four cell types between tumor and NATs.  $P$ -values were assessed using a two-sided unpaired Student's  $t$  test (Immu: \*\*\*\* $P < 0.0001$ , Endo: \*\*\*\* $P < 0.0001$ , CAFs: \*\* $P = 0.002$ ). **F** Multiplex immunofluorescence staining depicting the presence of four major cell components (CD45<sup>+</sup> immune cells, KRT5<sup>+</sup> epithelial cells, CD31<sup>+</sup> endothelial cells, and VIM<sup>+</sup> fibroblasts) in tumor and NATs of PSCC. Representative images include DAPI<sup>+</sup>

nuclei for reference. Scale: 50  $\mu\text{m}$ . **G** Multiplex immunofluorescence depicting the distribution of five major immune subpopulations (CD4<sup>+</sup> T cells, CD8<sup>+</sup> T cells, CD86<sup>+</sup> antigen-presenting cells, CD20<sup>+</sup> B cells, CD56<sup>+</sup> natural killer cells) in tumor and NATs of PSCC. Representative images include DAPI<sup>+</sup> nuclei for reference. Scale: 200  $\mu\text{m}$ . **H** Quantification of CD4<sup>+</sup>, CD8<sup>+</sup>, CD86<sup>+</sup>, CD20<sup>+</sup> and CD56<sup>+</sup> cells per area in paired tumor and NATs regions in PSCC ( $n = 6$ ).  $P$ -values were assessed using a two-sided paired Student's  $t$  test (CD4<sup>+</sup>: \*\*\*\* $P < 0.0001$ , CD8<sup>+</sup>: \*\*\* $P = 0.0002$ , CD86<sup>+</sup>: \*\*\* $P = 0.0002$ , CD20<sup>+</sup>: \*\*\*\* $P < 0.0001$ , CD56<sup>+</sup>: \*\* $P = 0.0053$ ). **I** UMAP plot comparing the TME composition in PSCC with other squamous cell carcinomas, including HNSCC (GSE103322), NPC (GSE150430), and cSCC (GSE144236). **J** Bar graph showing the relative proportions of the four cell types across these tumor types. *PN* PSCC adjacent normal tissue, *PT* PSCC tumor tissue. *NATs* Normal adjacent tissues. *HNSCC*: Head and neck squamous cell carcinoma, *NPC* Nasopharyngeal carcinoma, *cSCC* Cutaneous squamous cell carcinoma. Data are presented as mean  $\pm$  s.e.m. ns: not significant ( $P > 0.05$ ). Source data are provided as a Source Data file.

clinical outcomes reinforces the relevance of using this validation cohort for further analysis.

Tertiary lymphoid structures (TLSs), which are immune cell aggregates of B cells and T cells that form outside secondary lymphoid organs (SLOs) in response to chronic inflammation or infection<sup>30,31</sup>, have been associated with improved survival outcomes in several cancers, including melanoma<sup>32</sup>, renal cell carcinoma<sup>33</sup>, and sarcoma<sup>34</sup>. In our validation cohort, TLSs were significantly more enriched in tumor regions compared to adjacent non-tumor areas (Fig. 2H, I and Supplementary Fig. 3A). Notably, the density of TLSs per tumor area was significantly higher in HPV<sup>+</sup> PSCC compared to HPV<sup>-</sup> cases (Fig. 2J). Further analysis showed a significant enrichment of CD20<sup>+</sup> B cells within TLS in HPV<sup>+</sup> PSCC tumors compared to HPV<sup>-</sup> cases, while CD3<sup>+</sup> T cell numbers within TLSs remained similar between the two groups (Fig. 2K). mIF staining for CD3, CD20, and CD38 confirmed that TLSs in HPV<sup>+</sup> PSCC contained significantly higher numbers of CD20<sup>+</sup> B cells and CD38<sup>+</sup> activated B cells/plasma cells compared to TLSs in HPV<sup>-</sup> PSCC (normalized by tumor area to account for sample variability) (Fig. 2L, M). These findings indicate that HPV<sup>+</sup> PSCC is associated with a higher prevalence of TIL-Bs and TLSs, contributing to a distinct immune microenvironment compared to HPV<sup>-</sup> cases.

### IgA levels are increased in HPV<sup>+</sup> PSCC and correlate with improved survival

To further characterize TIL-Bs in PSCC, we bioinformatically isolated 12,724 TIL-Bs from 23 tumor samples, including 4459 cells from HPV<sup>-</sup> tumor and 8,625 from HPV<sup>+</sup> tumor (Fig. 3A). Based on the expression of key marker genes, we identified four distinct TIL-B clusters in PSCC: BACH2<sup>+</sup> or BACH2<sup>-</sup> Memory B cells (C1-C2, CD79A<sup>+</sup>MS4A1<sup>+</sup>SDC1<sup>+</sup>CD24<sup>+</sup>), plasma cells (C3, CD79A<sup>+</sup>MS4A1<sup>+</sup>CD24<sup>+</sup>CD38<sup>+</sup>SDC1<sup>+</sup>) and plasmablasts (C4, CD79A<sup>+</sup>MS4A1<sup>+</sup>MZB1<sup>+</sup>CD38<sup>+</sup>MKI67<sup>+</sup>) (Fig. 3A-C). Given the observed higher proportion and number of TIL-Bs in HPV<sup>+</sup> PSCC (Figs. 2D, 3D), we next investigated the functional impact of this increased B cell infiltration in HPV<sup>+</sup> PSCC. To this end, we performed differential gene expression analysis of TIL-Bs between HPV<sup>+</sup> and HPV<sup>-</sup> PSCC from the scRNA-seq datasets (Fig. 3E). TIL-Bs were divided into HPV<sup>+</sup> and HPV<sup>-</sup> groups to minimize analytical bias. This analysis revealed significantly higher expression of immunoglobulin-related genes such as *IGHG2*, *IGLC2* and *IGHA1* in TIL-Bs of HPV<sup>+</sup> PSCC compared to HPV<sup>-</sup> PSCC (Fig. 3E). The top differentially expressed genes were primarily associated with biological processes related to immunoglobulin-mediated and humoral immune responses (Fig. 3F).

Recent studies have demonstrated that plasma cells in tumors produce immunoglobulins that shape anti-tumor immune responses<sup>35</sup>, with different immunoglobulin isotypes driving distinct immune responses within the tumor microenvironment<sup>35,36</sup>. To further investigate this in PSCC, we performed bulk B cell receptor sequencing (bulk

BCR-seq) on 20 fresh tumor tissues (P11-P30). Library construction failed in 4 cases due to the limited residual tumor tissues, resulting in 16 samples (8 HPV<sup>-</sup> and 8 HPV<sup>+</sup>) available for downstream analysis. Following quality control and data processing (see Methods), we found that IgG (70.44%) was the dominant immunoglobulin isotype, followed by IgA (25.66%), while IgE, IgD, and IgM were negligible (Supplementary Fig. 4A). Notably, the diversity of IgG, IgA, IgE and IgM IGH isotype was significantly higher in HPV<sup>+</sup> PSCC compared to HPV<sup>-</sup> PSCC (Supplementary Fig. 4B).

To validate these findings, we performed IHC staining for SDC1 (CD138, a plasma marker), IgA and IgG in our validation cohort of 85 PSCC patients (Supplementary Figs. 1A, 5A, C and Supplementary Table 3). IHC results were scored on a scale from 0 to 4, with higher scores reflecting higher staining intensity and the fraction of positive cells. The detailed scoring system used for CD138, IgA, and IgG in our study was summarized in (Methods). Notably, the proportion of CD138<sup>+</sup> signals (score  $\geq 3$ ) was significantly higher in HPV<sup>+</sup> PSCC (28/33; 84.84%) compared to HPV<sup>-</sup> PSCC (14/52; 26.92%) (Fig. 3G). Similarly, IgA<sup>+</sup> signals (score  $\geq 3$ ) was also significantly elevated in HPV<sup>+</sup> PSCC (26/33; 78.78%) relative to HPV<sup>-</sup> PSCC (2/52; 3.84%) (Fig. 3H). In contrast, the proportion of IgG<sup>+</sup> signals (score  $\geq 3$ ) was comparable between HPV<sup>+</sup> (19/33; 57.57%) and HPV<sup>-</sup> PSCC (29/52; 55.76%) (Fig. 3I). Besides, the mean IHC score of CD138 and IgA was significantly higher in HPV<sup>+</sup> PSCC compared to HPV<sup>-</sup> PSCC (Fig. 3J, K), while IgG levels remained comparable between the two groups (Fig. 3L). In addition, ELISA was performed on freshly harvested tumor tissues and paired plasma samples from 13 PSCC patients (Supplementary Table 3). This analysis revealed a significant increase in tumor-associated IgA levels in HPV<sup>+</sup> PSCC, whereas IgG and plasma IgA/IgG levels showed no significant differences between HPV<sup>+</sup> and HPV<sup>-</sup> patients (Fig. 3M, N). When stratifying the 85 PSCC patients into high (score  $\geq 3$ ) and low (score  $\leq 2$ ) expression groups based on IHC staining for IgA, IgG, and CD138, only IgA expression was positively correlated with improved patient survival (Fig. 3O-Q). These findings suggest that HPV<sup>+</sup> PSCC exhibits significantly elevated IgA levels compared to HPV<sup>-</sup> PSCC, and that elevated IgA is associated with better survival outcomes in PSCC patients.

### Distinctive functional phenotypes of epithelial cells in HPV<sup>+</sup> and HPV<sup>-</sup> PSCC

Considering that transformed epithelial cells are the origin of PSCC and the primary targets of HPV infection<sup>1,6,7</sup>, we next sought to explore the intratumor heterogeneity within the epithelial compartments of PSCC. Our primary objective was to differentiate malignant epithelial cells from non-malignant epithelial ones in PSCC TME. Since malignant epithelial cells typically undergo large-scale chromosomal alterations during tumor progression, we used inferCNV<sup>23,37,38</sup> to estimate the sample-wise copy number variations (CNVs) of 12,748 epithelial cells

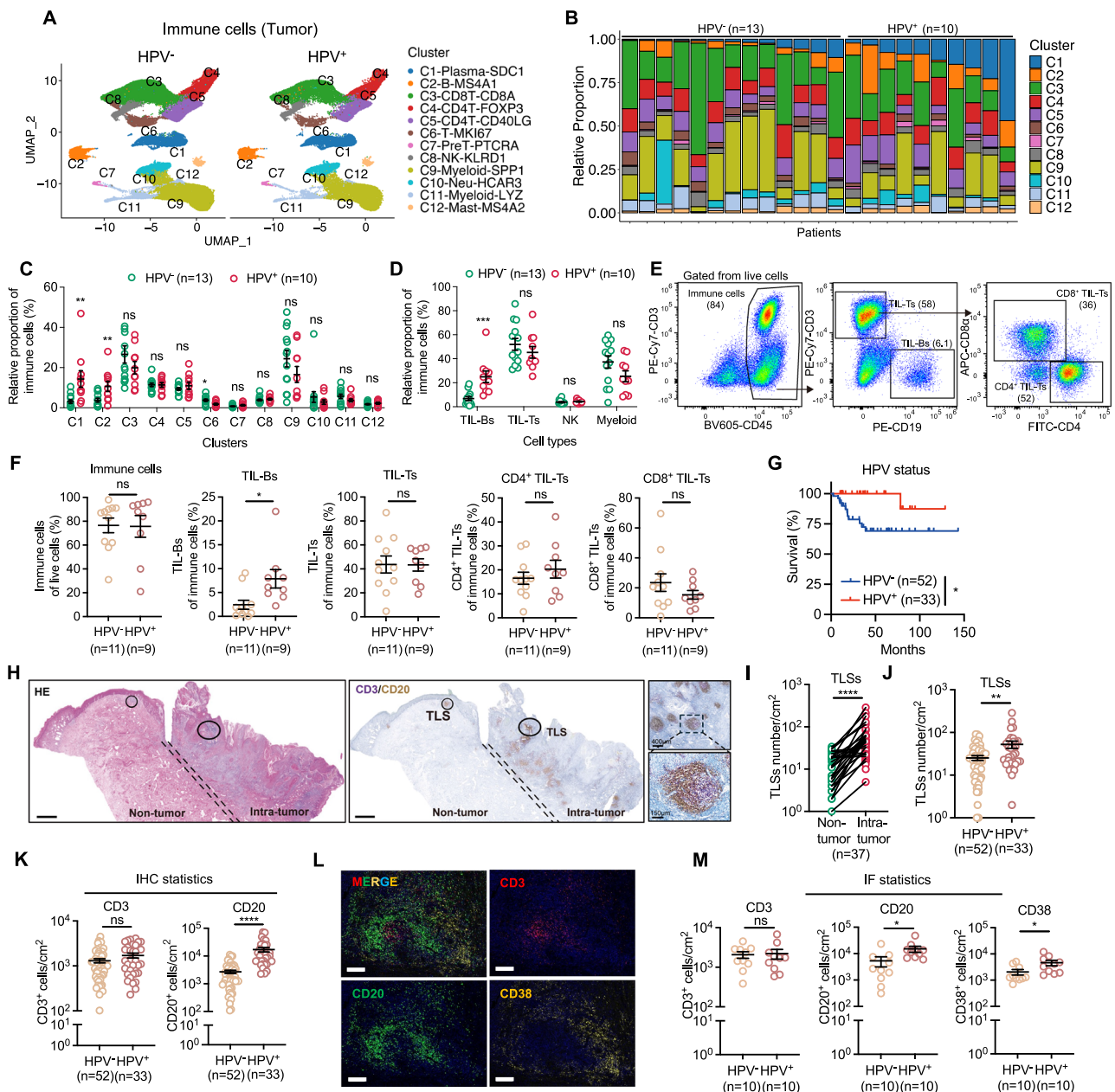


**Fig. 2 | Tumor-infiltrating B cells and tertiary lymphoid structures are enriched in HPV<sup>+</sup> PSCC.** **A** UMAP plot displaying 134,784 immune cells from scRNA-seq datasets of tumor specimens (HPV<sup>-</sup>, *n* = 13; HPV<sup>+</sup>, *n* = 10), including TIL-Bs (C1-C2), TIL-Ts (C3-C7), NK (C8) and myeloid-derived cells (C9-C12). **B** Relative abundance of each cluster in each PSCC patient. **C**, **D** Bar graph comparing the relative proportions of each cluster (**C**) and major immune types (**D**) between HPV<sup>-</sup> and HPV<sup>+</sup> PSCC. *P*-values were indicated for C1: *\*\*P* = 0.0063, C2: *\*\*P* = 0.01, C6: *\*\*P* = 0.0145 in (**C**) and TIL-Bs: *\*\*\*P* = 0.0007 in (**D**). **E** Gating strategy for FACS analysis in fresh PSCC specimens. **F** Histograms showing the relative proportions of total immune cells, TIL-Bs and TIL-Ts in fresh HPV<sup>-</sup> (*n* = 11) and HPV<sup>+</sup> (*n* = 9) PSCC tumors (*\*P* = 0.0151). **G** Overall survival curves of 85 patients with HPV<sup>-</sup> (*n* = 52) or HPV<sup>+</sup> (*n* = 33) PSCC (*\*P* = 0.0136). **H** Representative images of PSCC tumor sections with HE staining (left), double-plex IHC staining for CD20 and CD3 (middle), and TLSs (right), marked by black circles in both tumor and non-tumor regions. Scale bar: 2 mm (left and middle), 400 μm (upper right) and 150 μm (lower right).

**I** Quantification of TLSs per tumor area in non-tumor and intra-tumor regions in PSCC (*n* = 37) (*\*\*\*\*P* < 0.0001). **J** Number of TLSs per tumor area in HPV<sup>-</sup> (*n* = 52) and HPV<sup>+</sup> (*n* = 33) PSCC (*\*\*P* = 0.0029). **K** Quantification of the number of CD3<sup>+</sup> and CD20<sup>+</sup> within TLSs per tumor area in HPV<sup>-</sup> (*n* = 52) and HPV<sup>+</sup> (*n* = 33) PSCC tumor sections by IHC stained (*\*\*\*\*P* < 0.0001). **L** Representative immunofluorescence staining for CD3, CD20, CD38 and DAPI<sup>+</sup> nuclei within TLSs in HPV<sup>-</sup> and HPV<sup>+</sup> PSCC tumors. Scale bar: 200 μm. **M** Quantification of the number of CD3<sup>+</sup>, CD20<sup>+</sup>, and CD38<sup>+</sup> within TLSs per tumor area in HPV<sup>-</sup> (*n* = 10) and HPV<sup>+</sup> (*n* = 10) PSCC tumor sections by IF stained. (CD20: *\*P* = 0.0420, CD38: *\*P* = 0.0430). TIL-Bs: Tumor-infiltrating B cells. TIL-Ts: Tumor-infiltrating T cells. TLSs: tertiary lymphoid structures. A two-sided unpaired Student's *t* test was used in (**C**), (**D**), (**F**), (**J**), (**K**) and (**M**). A two-sided paired Student's *t* test for (**I**), and a two-sided log-rank (Mantel-Cox) test in (**G**). Data are presented as mean ± s.e.m. ns: not significant (*P* > 0.05). Source data are provided as a Source Data file.

isolated from the scRNA-seq datasets of PSCC tumor tissues and NATs from the discovery cohort (Fig. 1B). Epithelial cells from NATs, which showed no significant CNVs, were used as a reference. Epithelial cells exhibiting high CNVs scores were classified as malignant (Fig. 4A),

resulting in the identification of 9255 malignant cells for further analysis (see “Methods”).

Unsupervised clustering of the malignant cells revealed four distinct clusters (Fig. 4B). Among these, HPV<sup>+</sup> PSCC exhibited an

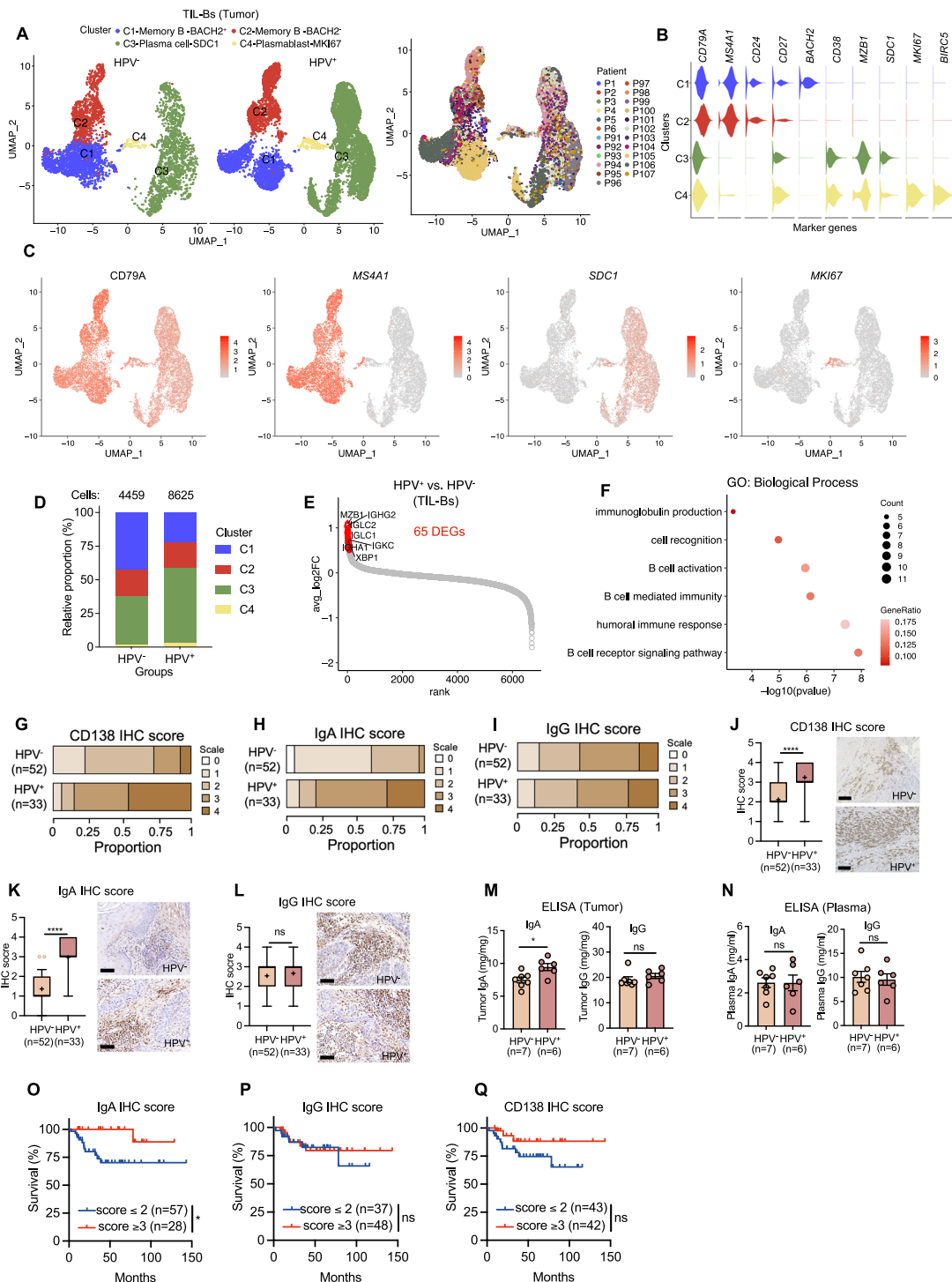
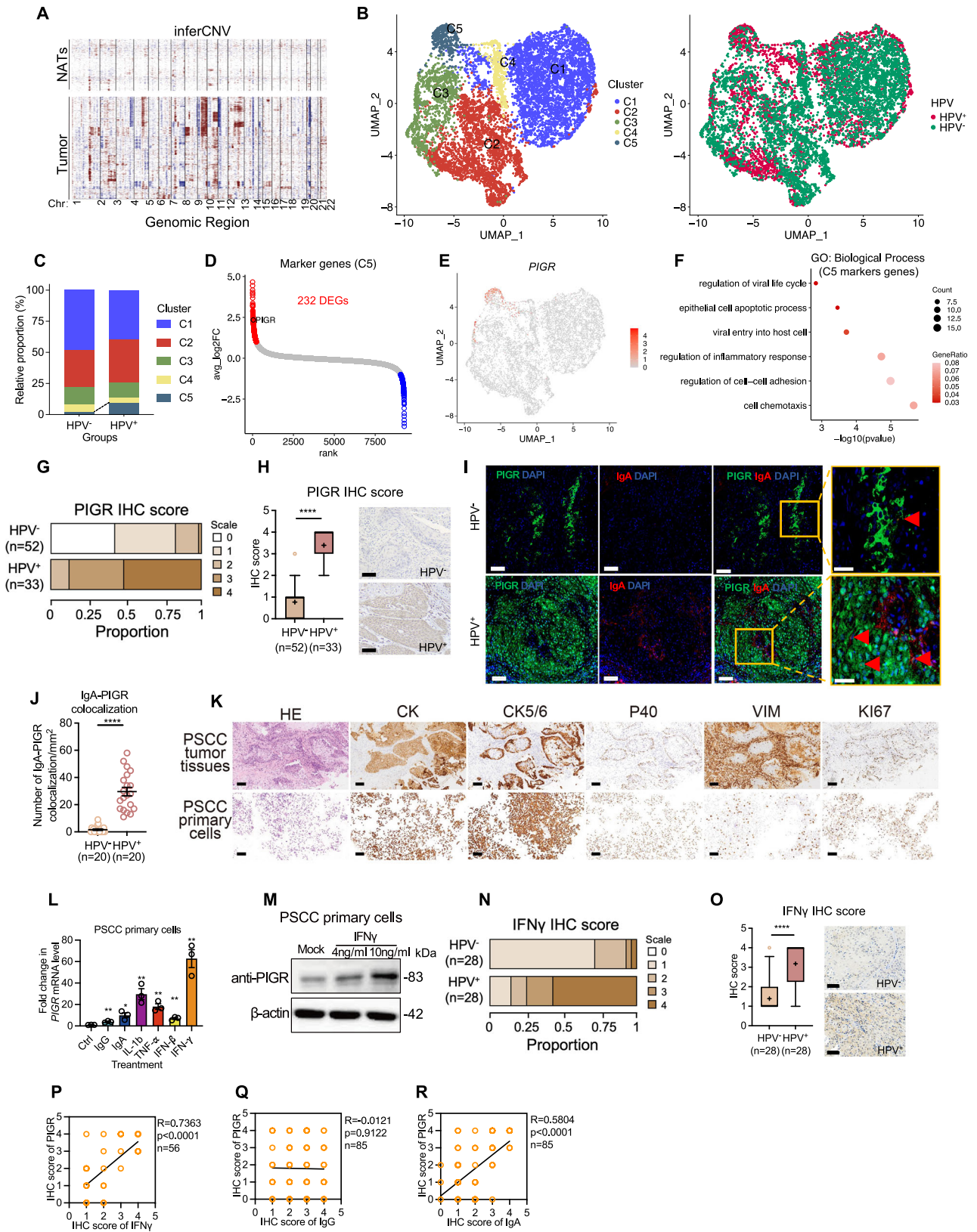


**Fig. 3 | IgA levels are increased in HPV<sup>+</sup> PSCC and correlate with improved survival.** **A** UMAP plot showing 12,724 TIL-Bs, categorized into four clusters, and colored by cell type (left) and patients (right). **B**, **C** Normalized expression of selected marker genes used to define each cluster (**B**) and cell types (**C**). **D** Bar graph showing the relative proportions of each cluster by HPV status. **E** Differential gene analysis comparing transcriptional profiles of TIL-Bs between HPV<sup>+</sup> and HPV<sup>-</sup> PSCC. Log<sub>2</sub> fold changes are shown for the top upregulated immunoglobulin-related genes. **F** Gene Ontology (GO) analysis highlighting the significantly upregulated genes in TIL-Bs from HPV<sup>+</sup> PSCC compared to HPV<sup>-</sup> PSCC. **G–I** Bar graphs depicting the relative proportion of immunohistochemistry (IHC) scores for CD138, IgA, and IgG in HPV<sup>-</sup> (*n* = 52) and HPV<sup>+</sup> (*n* = 33) PSCC tumor sections. IHC scores range from 0 to 4, as detailed in the Method section for scoring each marker. **J–L** Mean IHC score

and representative IHC staining images of CD138, IgA and IgG in HPV<sup>-</sup> (*n* = 52) and HPV<sup>+</sup> (*n* = 33) PSCC tumor specimens. *P*-values were assessed using a two-sided unpaired Student's *t* test (\*\*\*\**P* < 0.0001). Scale: 100 μm. **M**, **N** ELISA quantification of IgA and IgG levels in tumor tissues (**M**) paired plasma samples (**N**) from freshly harvested HPV<sup>-</sup> (*n* = 7) and HPV<sup>+</sup> (*n* = 6) PSCC. *P*-values were assessed using a two-sided unpaired Student's *t* test (\**P* = 0.0143). **O–Q** Overall survival curves of 85 PSCC patients, categorized by high (≥ 3) and low (≤ 2) IHC scores for IgA, IgG and CD138 in tumor sections. *P*-value was assessed using a two-sided log-rank (Mantel–Cox) test (\**P* = 0.0209). DEGs: Differentially expressed genes. Data are presented as mean ± s.e.m. ns: not significant (*P* > 0.05). Source data are provided as a Source Data file.



increased proportion of cluster 5 compared to HPV group (Fig. 4C). Go analysis of cluster 5 marker genes showed the various biological process, including “regulation of viral life cycle”, “epithelial cell apoptotic process” and “cell chemotaxis” (Fig. 4D, F). Notably, PIGR was specifically high expressed in the C5 cluster (Fig. 4D, E). PIGR is a receptor found on the surface of epithelial cells that regulates the transcytosis

of dimeric IgA and pentameric IgM, produced by local plasma cells<sup>39</sup>. Clinically, PIGR expression has been shown to vary across cancer types<sup>40–43</sup> and is associated with distinct patient outcomes and response to chemotherapy<sup>44</sup>. These findings highlight the unique biological behavior of PIGR<sup>+</sup> malignant cells (C5) and their potential relevance to HPV status in PSCC.

**Fig. 4 | PIGR<sup>+</sup> epithelial cells are enriched in HPV<sup>+</sup> PSCC and are induced by IFN $\gamma$ .**

**A** Heatmap displaying large-scale copy number variations (CNVs) for individual epithelial cells (rows) from NATs and tumors, with red indicating amplifications and blue indicating deletions. **B** UMAP plot of 9,255 malignant epithelial cells, showing five clusters colored by cell type (left) and HPV status (right). **C** Bar graph showing the relative proportions of each cluster by HPV status. **D** Differential gene analysis of cluster 5, with upregulated marker genes highlighted in red. **E** UMAP plot showing the cluster 5 specifically expressed genes *PIGR*. **F** Gene Ontology (GO) analysis of higher expressed marker genes in cluster 5. **G** Bar graph showing the relative proportion of IHC scores for PIGR in HPV<sup>-</sup> ( $n = 52$ ) and HPV<sup>+</sup> ( $n = 33$ ) PSCC tumor sections. **H** Mean IHC score and representative IHC staining images of PIGR in HPV<sup>-</sup> ( $n = 52$ ) and HPV<sup>+</sup> ( $n = 33$ ) PSCC tumor specimens (\*\*\*\* $P < 0.0001$ ). Scale: 100  $\mu\text{m}$ . **I** Representative immunofluorescence staining for PIGR, IgA and DAPI<sup>+</sup> nuclei in HPV<sup>-</sup> and HPV<sup>+</sup> PSCC tumor. Scale: 300  $\mu\text{m}$ . **J** Quantification of IgA-PIGR colocalization events in HPV<sup>-</sup> ( $n = 20$ ) and HPV<sup>+</sup> ( $n = 20$ ) PSCC samples (\*\*\*\* $P < 0.0001$ ). **K** Representative H&E and IHC staining for malignant epithelial

differentiation (CK, CK5/6, VIM and Ki67) and squamous cell origin (P40) in PSCC tumor tissues (top) and PSCC patient derived primary cells (bottom). Scale: 200  $\mu\text{m}$ . **L** Quantitative analysis of *PIGR* mRNA level with various factors treatment ( $n = 3$  independent experiments, IgA: \*\* $P = 0.0036$ , IgA: \* $P = 0.0190$ , IL-1 $\beta$ : \*\* $P = 0.0052$ , TNF- $\alpha$ : \*\* $P = 0.0029$ , IFN- $\beta$ : \*\* $P = 0.0028$ , IFN- $\gamma$ : \*\* $P = 0.0018$ ). **M** Quantitative analysis of PIGR protein level with IFN $\gamma$  treatment. **N** Bar graph showing the relative proportions of IHC scores for IFN $\gamma$  in HPV<sup>-</sup> ( $n = 28$ ) and HPV<sup>+</sup> ( $n = 28$ ) PSCC tumor sections. **O** Mean IHC score and representative IHC staining images of IFN $\gamma$  in HPV<sup>-</sup> ( $n = 28$ ) and HPV<sup>+</sup> ( $n = 28$ ) PSCC tumor specimens (\*\*\*\* $P < 0.0001$ ). Scale: 100  $\mu\text{m}$ . **P–R** Pearson correlation analysis of IHC scores between PIGR and IFN $\gamma$  (**P**), PIGR and IgG (**Q**), PIGR and IgA (**R**) in PSCC tumor sections (\*\*\*\* $P < 0.0001$ ). A two-sided unpaired Student's  $t$  test was used in (**H**), (**J**), (**L**) and (**O**). Pearson Correlation analysis with two-tailed was used in (**P–R**). Data are presented as mean  $\pm$  s.e.m. ns: not significant ( $P > 0.05$ ). Source data are provided as a Source Data file.

**PIGR<sup>+</sup> epithelial cells are enriched in HPV<sup>+</sup> PSCC**

To validate the enrichment of PIGR<sup>+</sup> epithelial cells in HPV<sup>+</sup> PSCC, we performed IHC staining to assess PIGR protein levels in tumor sections from 33 HPV<sup>+</sup> and 52 HPV<sup>-</sup> PSCC patients (Supplementary Fig. 5D and Supplementary Table 3). The proportion of PIGR<sup>+</sup> signals (score  $\geq 3$ ) was significantly higher in HPV<sup>+</sup> PSCC (29/33; 87.87%) compared to HPV<sup>-</sup> PSCC (1/52; 1.92%) (Fig. 4G). In addition, the average PIGR expression level was significantly elevated in HPV<sup>+</sup> PSCC compared to HPV<sup>-</sup> PSCC (Fig. 4H). Using mIF staining, we further examined the colocalization of IgA and PIGR (Supplementary Table 3). The number of IgA-PIGR colocalization events was significantly increased in HPV<sup>+</sup> PSCC compared to HPV<sup>-</sup> controls (Fig. 4I, J), suggesting an increased interaction between IgA and PIGR in HPV<sup>+</sup> PSCC.

To investigate the factors driving PIGR expression in HPV<sup>+</sup> PSCC, we isolated malignant epithelial cells from a PSCC patient's tumor lesions, cultured these patient-derived primary cells in conditioned medium and validated their proliferative and tumorigenic characteristics (Fig. 4K). These cells were treated with various stimuli, including immunoglobulins (dominated IgA and IgG in PSCC) and proinflammatory cytokines (e.g., IFN- $\gamma$ , TNF, IL-1), based on prior studies<sup>45</sup>. Among the treatments, IFN- $\gamma$  induced the highest increase in *PIGR* mRNA expression (Fig. 4L), which was further confirmed by Western blot analysis showing significant upregulation of PIGR protein levels in response to IFN- $\gamma$  treatment (Fig. 4M). Similar findings were observed in HeLa and HT29 cell lines (Supplementary Fig. 6A–D).

Given the strong induction of PIGR by IFN- $\gamma$  in our earlier experiments, we next sought to determine whether IFN- $\gamma$  expression was elevated in HPV<sup>+</sup> PSCC compared to HPV<sup>-</sup> PSCC. To address this, we performed IHC staining to assess IFN- $\gamma$  expression in tumor sections from 28 HPV<sup>+</sup> and 28 HPV<sup>-</sup> PSCC patients (Supplementary Fig. 5E and Supplementary Table 3). These cases were selected from the validation cohort based on the availability of suitable FFPE sections, as some samples had been partially or fully exhausted in prior analyses. The IHC analysis revealed a significantly higher proportion of IFN- $\gamma$ <sup>+</sup> cells (score  $\geq 3$ ) in HPV<sup>+</sup> PSCC (75%; 21/28) compared to HPV<sup>-</sup> PSCC (7.14%; 2/28) (Fig. 4N). In addition, the mean IHC score of IFN- $\gamma$  was markedly higher in HPV<sup>+</sup> PSCC (Fig. 4O). Further correlation analysis indicated a positive relationship between IFN- $\gamma$  and PIGR expression, as well as between IgA and PIGR, but not between IgG and PIGR, based on IHC staining in PSCC tumor sections (Fig. 5P–R). Collectively, these findings suggest that the enrichment of PIGR<sup>+</sup> epithelial cells in HPV<sup>+</sup> PSCC is likely driven by elevated levels of IFN- $\gamma$  within the tumor microenvironment, potentially enhancing IgA-PIGR interactions in HPV<sup>+</sup> tumors.

**High PIGR expression exerts anti-tumor effects in PSCC primary cells**

To explore the functional role of elevated PIGR expression in HPV<sup>+</sup> PSCC epithelial cells, we considered evidence from other cancer types

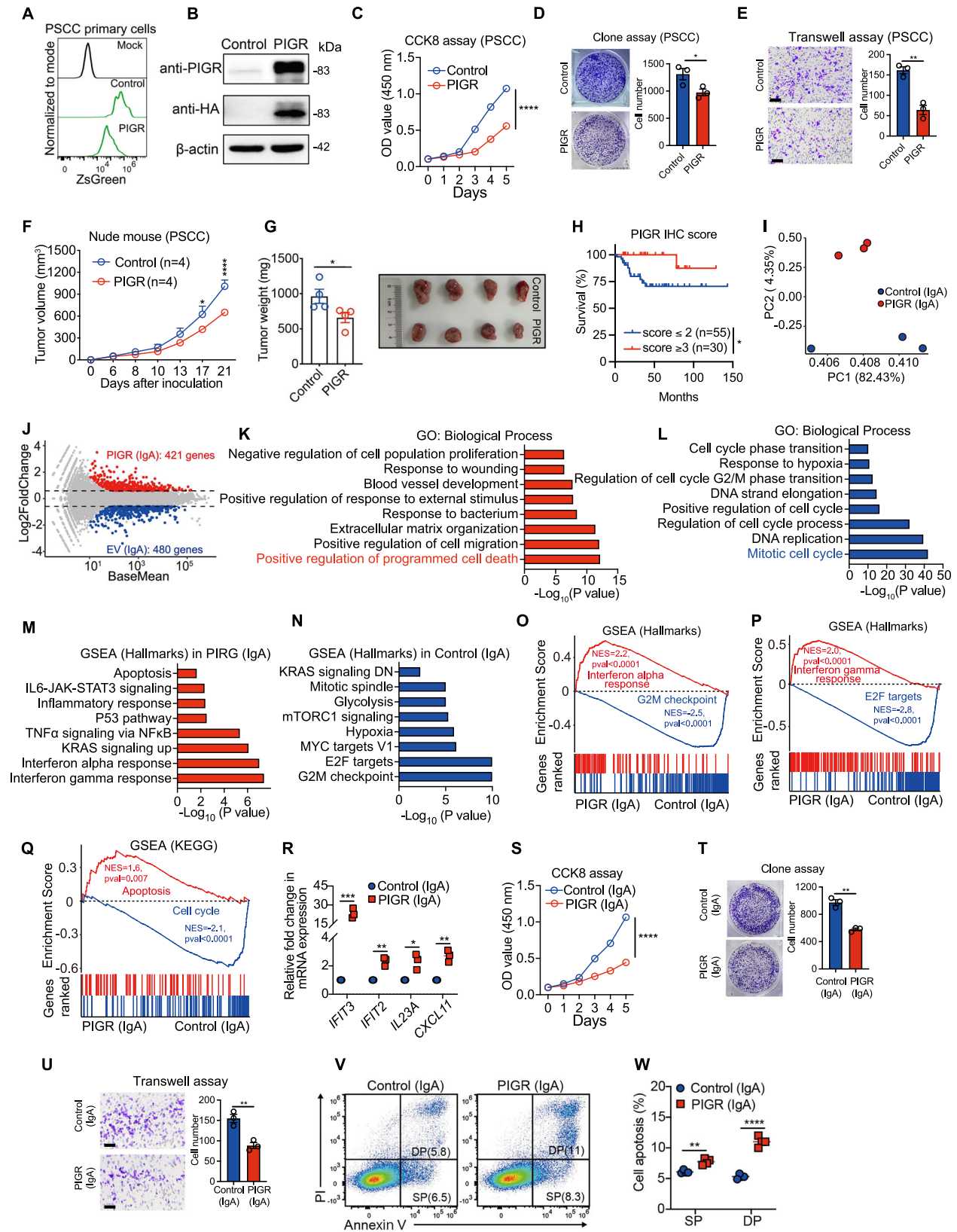
where reduced PIGR expression is linked to tumor progression, such as gastric adenocarcinoma<sup>46</sup>, non-small cell lung carcinoma<sup>47</sup>, and nasopharyngeal carcinoma<sup>43</sup>. Given that HPV<sup>+</sup> PSCC is associated with better clinical outcomes compared to HPV<sup>-</sup> cases, we hypothesized that higher PIGR expression in epithelial cells may have an anti-tumor effect in PSCC.

To test this hypothesis, we constructed lentiviral PIGR overexpression vectors and stably infected PSCC primary cells (Supplementary Fig. 7A). Following infection, ZsGreen-positive cells were sorted by flow cytometry to select cells with stable and high PIGR expression (Supplementary Fig. 7B). Successful overexpression of PIGR was confirmed through flow cytometry and Western blot analysis (Fig. 5A, B). We then assessed the impact of PIGR overexpression on cell proliferation and migration. Compared to the control cells, PIGR-overexpressing PSCC primary cells showed reduced proliferation and colony formation (Fig. 5C, D) and decreased migration capacity in transwell assays (Fig. 5E). To further investigate the role of PIGR in vivo, we subcutaneously implanted control- and PIGR-overexpressing PSCC primary cells into nude mice and monitored the tumor growth every other day. As expected, PIGR-overexpressing PSCC cells led to significantly slower tumor growth and lower tumor weight compared to controls (Fig. 5F, G). In addition, clinical correlation analysis in our cohort revealed that higher PIGR expression was associated with improved survival outcomes in PSCC patients (Fig. 5H). Taken together, these findings suggest that elevated PIGR expression in PSCC epithelial cells exerts an anti-tumor effect, both in vitro and in vivo, as demonstrated in immune-incompetent mouse models.

**High IgA-PIGR expression promotes anti-tumor activity in PSCC primary cells**

Given the elevated levels of TIL-Bs, IgA, and PIGR<sup>+</sup> malignant epithelial cells in the HPV<sup>+</sup> PSCC tumor microenvironment, we hypothesized that the PIGR-mediated transcytosis of IgA might establish an immune-epithelial axis with potential anti-tumor effects. To test this hypothesis, we conducted RNA sequencing on IgA-stimulated PSCC primary cells, comparing PIGR-overexpressing cells with controls. Principal component analysis (PCA) confirmed the high quality and reproducibility of the sequencing data (Fig. 5I). Gene ontology (GO) analysis of differentially expressed genes revealed that IgA-PIGR groups exhibited significant upregulation of pathways, such as 'positive regulation of programmed cell death' (Fig. 5J, K). Conversely, genes related to the 'mitotic cell cycle' and 'DNA replication' were notably downregulated in the IgA-PIGR group (Fig. 5J, L).

To further validate these findings, we performed gene set enrichment analysis (GSEA). The IgA-PIGR group exhibited significant enrichment in immune-related pathways, including 'interferon alpha response,' 'interferon gamma response,' and 'apoptosis' (Fig. 5M, O–Q). In contrast, the control group displayed enrichment in cell



cycle-related pathways such as ‘G2M checkpoint’ and ‘E2F targets’ (Fig. 5N, O–Q). In addition, qPCR analysis confirmed that immune-related genes such as *IFIT3* and *IFIT2* (IFN-stimulated genes), *IL23A* (interleukin), and *CXCL11* (chemokine) were significantly upregulated in the IgA-treated PIGR group (Fig. 5R). Our results align with findings

from studies on endometrial<sup>48</sup> and ovarian cancer<sup>41</sup> cells, where IgA transcytosis via PIGR also triggers immune responses and promotes apoptosis, suggesting a conserved mechanism across cancer types. Notably, in PSCC cells, we observed specific downregulation of pathways such as ‘Cell cycle,’ ‘G2M checkpoint,’ and ‘E2F targets,’ which

**Fig. 5 | PIGR-mediated IgA transcytosis promotes anti-tumor activity in PSCC primary cells.** **A** FACS analysis of lentivirus-based PIGR overexpression in PSCC primary cells, including wild-type (mock), empty vector-overexpressed (control) and PIGR-overexpressed (PIGR) groups. **B** Western blot detection of PIGR expression. **C–E** CCK8 cell proliferation (**C**), colony formation (**D**), and transwell migration (**E**) assays in control- and PIGR-overexpressing groups ( $n = 3$  independent experiments, \*\*\*\* $P < 0.0001$ , \* $P = 0.0497$ , \*\* $P = 0.0023$ , respectively). Scale: 100  $\mu\text{m}$ . **F, G** Tumor growth curves (**F**) and tumor weights (**G**) in nude mice subcutaneously injected with control- or PIGR-overexpressing PSCC primary cells ( $n = 4$  independent experiments). \* $P = 0.0258$ , \*\*\*\* $P < 0.0001$  in (**F**) and \* $P = 0.0497$  in (**G**). **H** Kaplan-Meier survival curve of 85 PSCC patients grouped by high ( $\geq 3$ ) and low ( $\leq 2$ ) PIGR IHC scores in PSCC tumor sections (\* $P = 0.0236$ ). **I–Q** RNA-Seq transcriptome profiling of control- and PIGR-overexpressing PSCC primary cells treated with IgA treatment. **I** Principal component analysis (PCA) of both groups. **J** Differential gene analysis showing DEGs in both groups. **K, L** Gene Ontology (GO) analysis of upregulated DEGs in the PIGR-IgA group (**K**) and the control-IgA group (**L**). **M–Q** Gene set enrichment analysis (GSEA) showing pathways significantly

enriched in the PIGR-IgA group (**M, O–Q**) or the control-IgA group (**N, O–Q**). **R** qPCR validation of selected interferon-stimulated genes (*IFIT2*, *IFIT3*), inflammatory genes (*IL23A*), and chemokines (*CXCL11*) upregulated in the PIGR-IgA group ( $n = 3$  independent experiments. *IFIT3*: \*\*\*\* $P = 0.0006$ , *IFIT2*: \*\* $P = 0.0016$ , *IL23A*: \* $P = 0.0138$ , *CXCL11*: \*\* $P = 0.0021$ ). **S–W** Cell proliferation (**S**), colony formation (**T**), and transwell migration (**U**) assays were performed on IgA-treated control- and PIGR- groups ( $n = 3$  independent experiments, \*\*\*\* $P < 0.0001$ , \*\* $P = 0.0010$ , \*\* $P = 0.0059$ , respectively). **V, W** Representative FACS analysis of PI/Annexin V staining (**V**) and quantification of early apoptosis (SP) and late apoptosis (DP) percentages (**W**) in IgA-treated control- and PIGR- groups ( $n = 4$  independent experiments, SP: \*\* $P = 0.0011$ , DP: \*\*\*\* $P < 0.0001$ ). DEGs: differentially expressed genes. A two-sided unpaired Student's *t* test was used in (**D**), (**E**), (**G**), (**R**), (**T**), (**U**) and (**W**). A two-way ANOVA test with multiple comparisons was used in (**C**), (**F**), and (**S**). Two-sided log-rank (Mantel–Cox) test was used in (**H**). Data are presented as mean  $\pm$  s.e.m. ns: not significant ( $P > 0.05$ ). Source data are provided as a Source Data file.

were not significantly impacted in endometrial or ovarian cancer. This suggests that the IgA-PIGR axis may have additional inhibitory effects on cell cycle regulation in PSCC, contributing to its anti-tumor activity in this context.

To assess the functional role of the IgA-PIGR axis in regulating cell behavior, we performed cell proliferation, migration, and apoptosis assays. PSCC primary cells, either PIGR-overexpressing or control, were treated with IgA, and the effects on cell proliferation were assessed using CCK-8 assays and colony formation assays. IgA-treated PIGR-overexpressing cells exhibited significantly reduced proliferation and colony formation compared to the IgA-treated control group (Fig. 5S, T). Migration assays using a transwell system demonstrated that PIGR-overexpressing cells had significantly reduced migration capacity compared to controls (Fig. 5U).

We extended these findings by investigating the effects of IgA-PIGR interaction in the A549 lung adenocarcinoma cell line, which naturally expresses high levels of PIGR. The results mirrored those in PSCC cells, showing reduced growth and migration upon IgA treatment in PIGR-expressing cells (Supplementary Fig. 8A–D). Moreover, apoptosis assays using PI/Annexin V staining showed that IgA treatment significantly increased apoptosis in PIGR-overexpressing PSCC primary cells compared to controls (Fig. 5V, W). These findings demonstrate that the IgA-PIGR axis has potent anti-tumor effects in PSCC epithelial cells, impacting key processes such as cell proliferation, migration, and apoptosis. This suggests a critical role for IgA-PIGR interaction in mediating anti-tumor responses in the HPV<sup>+</sup> PSCC tumor microenvironment.

### High IgA-PIGR expression promotes anti-tumor activity in vivo

To assess the anti-tumor role of the IgA-PIGR axis in vivo, we utilized the MC38 colon carcinoma model, as human PSCC primary cells cannot be used in immune-competent C57BL/6 mice. While the MC38 model has limitations due to its low B-cell and plasma cell infiltration<sup>49–51</sup>, it remains useful for studying the downstream effects of IgA-PIGR interactions on tumor cells, particularly in an immunocompetent setting. In light of this, we hypothesized that the IgA-PIGR axis may also play an anti-tumor role in MC38 tumors.

To test this, we generated PIGR-overexpressing MC38 cells using lentivirus-based PIGR vectors. Cells with stable PIGR expression were selected via ZsGreen-positive sorting through flow cytometry (Supplementary Fig. 7C). Successful PIGR overexpression in MC38 cells was confirmed by both flow cytometry and Western Blot (Supplementary Fig. 7D, E). Next, we subcutaneously inoculated control and PIGR-overexpressing MC38 cells into wild-type C57BL/6 mice and administered anti-CD20 antibodies (aCD20 mAb) at the time of tumor implantation and at 10-day intervals to deplete B cells (Fig. 6A). We monitored tumor growth every other day and observed that depletion

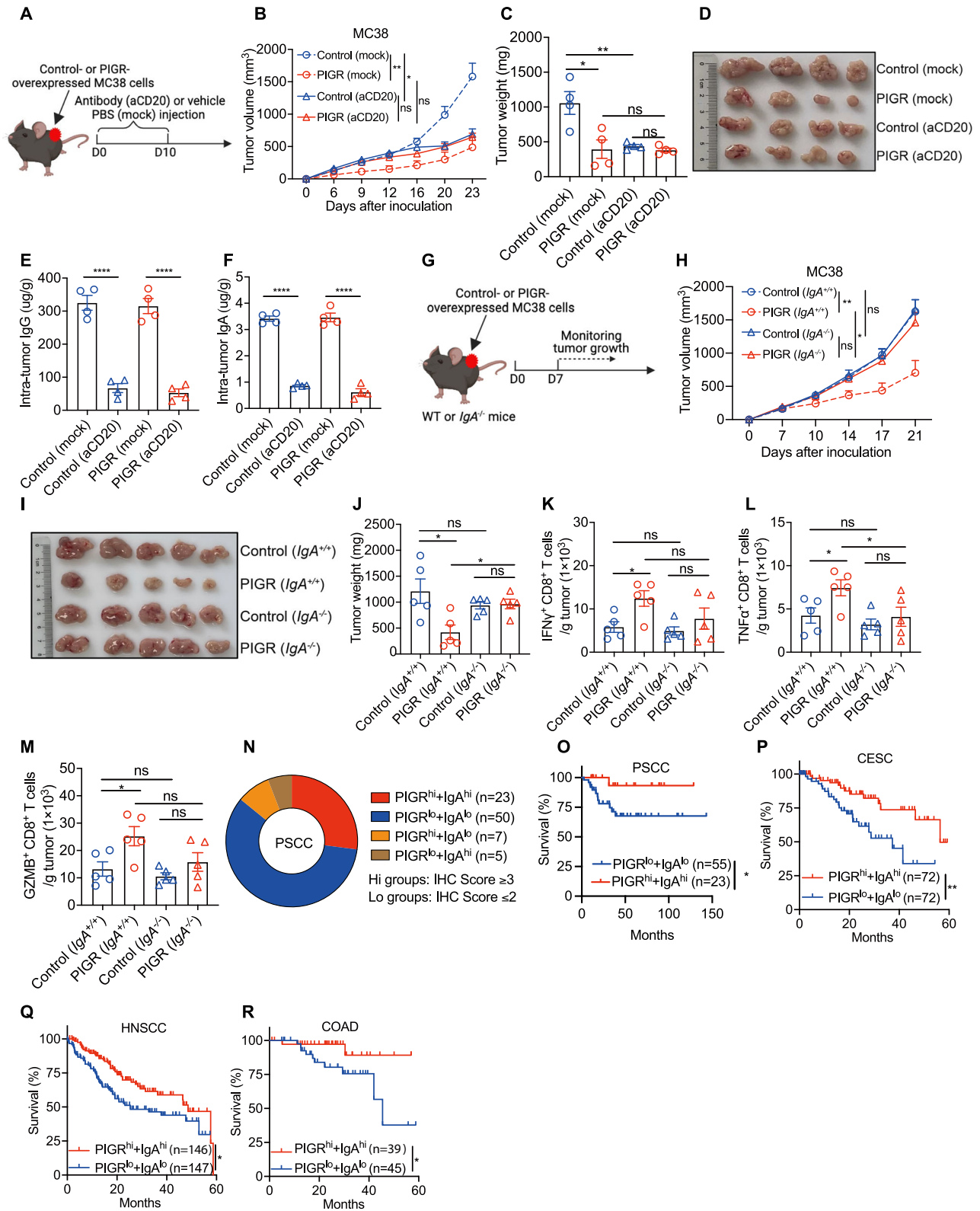
of CD20<sup>+</sup> B cells from the blood and spleen effectively reduced IgA and IgG levels in tumor tissues (Fig. 6E, F). B cell depletion via anti-CD20 treatment at earlier time-point significantly inhibited MC38 tumor growth, consistent with previous studies showing B cell-deficient mice suppresses MC38 tumors<sup>52</sup>. In wild-type mice, PIGR-overexpressing MC38 cells exhibited significantly slower tumor growth compared to controls, but this growth inhibition was abolished in mice treated with aCD20 mAb (Fig. 6B–D), suggesting that CD20<sup>+</sup> B cells contribute to PIGR-mediated anti-tumor activity in the MC38 model.

To specifically assess whether the IgA-PIGR axis mediates anti-tumor effect, we inoculated control and PIGR-overexpressing MC38 cells into wild-type and IgA-deficient (*IgA*<sup>-/-</sup>) mice (Fig. 6G). The absence of IgA alone did not significantly affect MC38 tumor growth (Fig. 6H), indicating that IgA may not be the primary driver of tumor suppression in this model. This aligns with the limited B cell infiltration and restricted isotype-switched immune responses typically seen in MC38 tumors, where IgA is more likely sourced from peripheral sites rather than produced locally by tumor-infiltrating B cells. However, our focus was on the downstream effects of IgA-PIGR interaction. We observed enhanced anti-tumor effects with PIGR overexpression, which were notably reduced in *IgA*<sup>-/-</sup> mice, indicating the necessity of IgA for PIGR-mediated tumor suppression (Fig. 6H–J). Flow cytometry analysis further showed increased infiltration of cytotoxic CD8<sup>+</sup> T cells in WT mice bearing PIGR-overexpressing tumors, an effect not seen in *IgA*<sup>-/-</sup> mice (Fig. 6K–M and Supplementary Fig. 9A). These findings underscore the critical role of an intact IgA-PIGR axis in driving anti-tumor responses in the MC38 model, highlighting IgA's contribution to PIGR-mediated tumor suppression.

### High IgA-PIGR expression correlates with improved survival in PSCC and mucosal-associated carcinoma

To explore the clinical relevance of our findings, we investigated whether elevated levels of IgA and PIGR in the TME correlate with improved patient survival in PSCC and other cancers. We performed IHC analysis of IgA and PIGR expression in tumor tissues from 85 PSCC patients. The results showed that 27.05% of patients (23/85) exhibited high expression of both IgA and PIGR, while 58.82% (50/85) had low expression of both. In addition, 8.23% (7/85) displayed high IgA but low PIGR expression, and 5.88% (5/85) showed high PIGR but low IgA expression (Fig. 6N). Notably, patients with high expression of both IgA and PIGR demonstrated significantly improved survival outcomes (Fig. 6O).

To extend our findings beyond PSCC, we analyzed *IgA* and *PIGR* transcript expression in various cancers using data from The Cancer Genome Atlas (TCGA), including bladder, breast, colon, cervix uteri, esophagus, head and neck, and lung cancers. While no significant correlation with overall survival was observed in cancers such as



bladder, breast, esophageal, and lung, mucosal-associated carcinomas –such as cervical squamous cell carcinoma (CESC) (Fig. 6P), head and neck squamous cell carcinoma (HNSCC) (Fig. 6Q), and colon adenocarcinoma (COAD) (Fig. 6R)—showed a positive association between elevated IgA and PIGR expression and improved survival. These findings suggest that the IgA-PIGR axis plays a role in favorable clinical outcomes in PSCC, particularly HPV<sup>+</sup> cases, and may also contribute to improved survival in other mucosal-associated carcinomas.

## Discussion

In this study, we conducted an integrated analysis of the tumor microenvironment (TME) in HPV<sup>+</sup> and HPV<sup>-</sup> PSCC patients to better understand immune-epithelial interactions and the mechanisms underlying the improved prognosis observed in HPV<sup>+</sup> cases. Using single-cell RNA sequencing, immunohistochemistry (IHC), mouse genetic models, and xenograft experiments, we profiled immune cell populations and their interactions with epithelial cells across a cohort

**Fig. 6 | PIGR-mediated IgA transcytosis promotes anti-tumor activity in vivo.** **A–D** Experimental schematic (**A**), tumor growth curves (**B**), tumor weight (**C**), and tumor images (**D**) of C57BL/6 wild-type mice subcutaneously inoculated with control- or PIGR-overexpressing MC38 cells. Anti-CD20 antibodies (250 µg per mouse) were administered at the time of tumor cell implantation and at 10-day intervals to deplete B cells ( $n = 4$  independent experiments).  $^{*}P = 0.0271$  and  $^{**}P = 0.0057$  in (**B**),  $^{*}P = 0.0195$  and  $^{***}P = 0.0093$  in (**C**). **E, F** ELISA quantification of intra-tumor IgG (**E**) and IgA (**F**) levels from panel (**D**).  $n = 4$  independent experiments ( $^{****}P < 0.0001$ ). **G–J** Schematic of experimental design (**G**), tumor growth curves (**H**), tumor images (**I**) and tumor weight (**J**) in WT ( $IgA^{+/+}$ ) and IgA-deficient ( $IgA^{-/-}$ ) mice inoculated subcutaneously with control- and PIGR-overexpressing MC38 cells ( $n = 5$  independent experiments).  $^{*}P = 0.0110$  and  $^{**}P = 0.0063$  in (**H**),  $^{*}P = 0.0205$  (between Control ( $IgA^{+/+}$ ) and PIGR ( $IgA^{+/+}$ )) and  $^{**}P = 0.0115$  (between PIGR ( $IgA^{+/+}$ ) and PIGR ( $IgA^{-/-}$ )) in (**J**). **K–M** Quantification of tumor infiltrating IFN $\gamma^{+}$ CD8 $^{+}$  T cells (**K**), TNF $\alpha^{+}$ CD8 $^{+}$  T cells (**L**) and GZMB $^{+}$ CD8 $^{+}$  T cells (**M**) from panel (**I**).  $n = 5$  independent experiments,  $^{*}P = 0.0160$  in (**K**),  $^{*}P = 0.0362$  (between Control

( $IgA^{+/+}$ ) and PIGR ( $IgA^{+/+}$ )) and  $^{**}P = 0.0484$  (between PIGR ( $IgA^{+/+}$ ) and PIGR ( $IgA^{-/-}$ )) in (**L**),  $^{*}P = 0.0254$  in (**M**). **N** Pie chart showing the classification of 85 PSCC patients according to the IHC scores for PIGR and IgA in PSCC tumor sections. High expression groups: IHC score  $\geq 3$ . Low expression groups: IHC score  $\leq 2$ . **O** Kaplan-Meier survival curve for PSCC patients grouped by high or low co-expression of PIGR and IGA based on IHC scores ( $^{*}P = 0.0382$ ). **P–R** Correlation between overall survival and the transcripts of *PIGR* and *IgA* in patients from the TCGA database for CESC ( $^{**}P = 0.0044$ ) (**P**), HNSCC ( $^{*}P = 0.0410$ ) (**Q**) and CDAD ( $^{*}P = 0.0303$ ) (**R**). CESC: Cervical squamous cell carcinoma, HNSCC: Head and neck squamous cell carcinoma, COAD: Colon adenocarcinoma. A two-sided unpaired Student's *t* test was used in (**C**), (**E**), (**F**), (**J–M**). A two-way ANOVA test was used in (**B**) and (**H**). Two-sided log-rank (Mantel–Cox) test was used in (**O–R**). Data are presented as mean  $\pm$  s.e.m. ns: not significant ( $P > 0.05$ ). Figures (**A** and **G**) were created in BioRender. Pan, W. (2025) <https://biorender.com/udc23v6>. Source data are provided as a Source Data file.

of 85 PSCC patients. Our single-cell analysis revealed a significant enrichment of tumor-infiltrating B cells (TIL-Bs), tertiary lymphoid structures (TLSs), and IgA in the TME of HPV $^{+}$  PSCC compared to HPV $^{-}$  cases. Notably, we also identified an increased presence of PIGR $^{+}$  epithelial cells in HPV $^{+}$  tumors. Functional assays in vitro and in vivo using wild-type and IgA-deficient mice demonstrated that the IgA-PIGR axis plays a critical role in driving anti-tumor responses and improving survival. These findings provide mechanistic insights into HPV-associated immune modulation in PSCC and suggest that elevated IgA-PIGR levels could serve as a biomarker for clinical outcomes in PSCC and other mucosal-associated carcinomas.

Our study highlights the intricate immune-epithelial crosstalk in the PSCC TME, with a particular focus on the B cell-IgA-PIGR axis. While PIGR overexpression alone can activate downstream signaling pathways—potentially due to receptor clustering or constitutive activation—our data suggest that IgA binding to PIGR fine-tunes and amplifies these signals in ways that PIGR overexpression alone does not fully achieve. This interaction may enhance anti-tumor immunity by modulating epithelial responses, reinforcing the role of IgA-PIGR signaling in tumor suppression. Besides, the MC38 tumor phenotypes observed in the B cell clearance and  $IgA^{-/-}$  backgrounds are distinct. These differences suggest that B cells, including activated B cells, plasma cells, and those involved in antigen presentation, may influence the tumor microenvironment through mechanisms that are independent of IgA alone. Despite the baseline differences, overexpression of PIGR and the dominant IgA-PIGR axis significantly reduced tumor growth in the MC38 models, highlighting the distinct contributions of IgA in different contexts and underscores the role of the IgA-PIGR pathway in modulating tumor progression.

Current immunotherapies primarily aim to reactivate exhausted CD8 $^{+}$  T cells within the TME. However, our findings suggest that IgA can also inhibit tumor progression through non-specific transcytosis via PIGR $^{+}$  malignant epithelial cells. Recent studies have also shown that dimeric IgA undergoes transcytosis through PIGR $^{+}$  epithelial cancer cells and can be engineered to target intracellular mutated oncogenes, enhancing anti-tumor immunity in lung and colorectal cancers<sup>53</sup>. These findings highlight the potential of targeting both B-cell and T-cell responses in PSCC to improve therapeutic efficacy. A key unresolved question is whether the antibodies produced in HPV $^{+}$  and HPV $^{-}$  PSCC are primarily tumor-reactive or directed against HPV viral antigens. Studies in HPV $^{+}$  head and neck squamous cell carcinoma (HNSCC) have demonstrated that TIL-Bs produce antibodies targeting viral antigens such as E2, E6, and E7<sup>54</sup>. Whether a similar phenomenon occurs across HPV-associated mucosal carcinomas remains to be explored. Future studies should investigate the specificity and function of antibodies within the HPV $^{+}$  TME to better define their role in anti-tumor immunity.

## Methods

### Patient cohorts and sample allocation

A total of 107 penile squamous cell carcinoma (PSCC) cases were included in this study. Specimens were obtained from patients who underwent surgical excision at The First Affiliated Hospital of the University of Science and Technology of China. Written informed consent was obtained from all participants in accordance with the Declaration of Helsinki. Of the 107 cases, 60 archival FFPE samples (P31–P90) were collected prior to project initiation (2011–2021) and were primarily used for validation assays, including immunohistochemistry (IHC). In parallel, 47 fresh tumor cases were prospectively and consecutively collected between 2021 and 2025, serving as the main discovery cohort. Among these, 30 patients (P1–P30) contributed both FFPE and fresh tumor tissues, while an additional 17 patients (P91–P107) were accrued during the revision stage and specifically contributed fresh tumor tissues for scRNA-seq. In total, 28 samples (23 tumors and 5 NATs) passed scRNA-seq quality control, yielding 202,424 single cells for downstream analyses. Among the 23 tumor samples included in the scRNA-seq dataset, 11 samples (P1–P6 and P91–P95) have already been reported in our previously published work<sup>20</sup>.

Tissue allocation to assays was dictated solely by real-time availability and technical feasibility, without any pre-selection based on clinical or biological features. Fresh samples with sufficient viable tissue were prioritized for scRNA-seq, a tissue-consuming assay that precluded parallel flow cytometry. Flow cytometry was therefore performed on other consecutively accrued fresh tumors that met viability thresholds. For histologic validation, we examined an inclusive FFPE cohort of 90 consecutively accrued patients (P1–P90). To ensure accurate HPV classification, five archival cases with discordant results (p16-positive/HPV PCR-negative) were excluded, leaving 85 evaluable cases for IHC analyses.

### HPV status definition

HPV status in PSCC samples was determined using p16 immunohistochemistry (IHC) staining according to the recommendations of the International Society of Urological Pathology (ISUP), which recognizes p16 IHC as a standard method for detecting HPV infection and classifying penile tumors<sup>21</sup>. p16 positivity was defined as strong, diffuse nuclear and cytoplasmic staining in at least 70% of the tumor cells, based on validated criteria for multiple HPV-related cancers, including PSCC<sup>55</sup> and HNSCC<sup>26,27</sup>. For PCR-based confirmation, HPV-specific universal primers SPF1/GP6++ was used to detect a broad range of HPV types, including HPV 11, 16, 18, 31, 33, 34, 35, 39, 51, 52, 53, 56, 58, 61, and 66 following established protocols<sup>56</sup> (Supplementary Table 6). DNA was extracted from tumor samples using either fresh tissue ( $n = 47$ ) with the Animal Tissues/Cells Genomic DNA Extraction Kit (D1700, Solarbio), or FFPE samples ( $n = 60$ )

with the TIANamp FFPE DNA Kit (DP331, Tiangen). A PCR product with a ~180 bp band indicates HPV positivity, while no visible band indicates HPV negativity. Given the limited sensitivity of PCR in degraded FFPE tissues, HPV status was assessed using both p16 IHC and HPV PCR. Cases were classified as HPV-positive if they were p16-positive and showed an ~180 bp band on HPV PCR. Cases were considered HPV-negative if they were p16-negative and showed no PCR band.

### HPV DNA in Situ Hybridization Detection

HPV DNA was identified using the HPV detection kit (Triplex International Biosciences, HPV high-risk-20A). Tissue slices were first subjected to microwave treatment for 30 min, and then the slices were subjected to proteinase K digestion for 5 min, followed by probe hybridization (add 20  $\mu$ l of hybridization solution to each slice and add a coverslip). The slices were placed on a 95 °C heater for denaturation treatment for 5 min, and then were placed in a humidified box and incubated at 37 °C for 16 h. After that, diaminobenzidine (DAB) was used to develop color, and finally hematoxylin counterstaining was used to display the cell nuclei, alcohol dehydration, and neutral gum covered the slices.

### Immunohistochemistry (IHC)

IHC was performed retrospectively on patient tumor tissue sections against p16, CD3, CD20, CD138 (SDC1), IgA, IgG, PIGR and IFN- $\gamma$ . Owing to limited biospecimen availability, IHC staining was performed only once for each tumor sample. Tissues were fixed in 4% paraformaldehyde, followed by dehydration, paraffin embedding and sectioning. Slices were subjected to immunohistochemical staining. Specifically, specific marker-stained images were analyzed digitally with the image analysis software Image J to determine the amount or intensity of IHC staining by measuring the area of the IHC-stained cells or structure in the center of a tumor and in the invasive margin of the tumor. The tumor region was delineated by two trained pathologists. Specific markers expression was categorized by tumor cell IHC scoring: high expression (score = 4 or 3), low expression (score = 2 or 1) or no expression (score = 0). The following primary antibodies were used for immunohistochemical staining: mouse-anti-human p16 (MXB- bio, MAB-0673), mouse-anti-human CD3 (ZsBio, ZM-0417), mouse-anti-human-CD20 (ZsBio, ZM-0039), rabbit-anti-human CD138 (ZsBio, ZA-0584), rabbit-anti-human IgA (ZsBio, ZA-0446), rabbit-anti-human IgG (ZsBio, ZA-0448), rabbit-anti-human PIGR (Abram, ab96196), rabbit-anti-human IFN- $\gamma$  (Abram, ab25101).

The multiplex immunofluorescence staining protocol was performed as follows: First, 3- $\mu$ m-thick slices from formalin-fixed paraffin-embedded (FFPE) tissues were mounted on highly adhesive glass slices. The slices were then baked at 65 °C overnight, dewaxed using xylene, and rehydrated in a series of ethanol solutions. Following this, heat-induced antigen retrieval was carried out with citrate buffer (Akoya Biosciences, NEL811001KT). After a 10 min blocking step, slices were incubated with primary antibodies at room temperature for 60 min. Unbound antibodies were removed by washing with TBST (0.1% Tween 20), and a fluorescein-conjugated secondary antibody was applied. Finally, nuclei were counterstained with DAPI for 5 min, and the slices were mounted with an antifade medium and stored at 4 °C in the dark. Primary antibodies were mouse-anti-human KRT5 (ZsBio, TA800727), mouse-anti-human CD45 (ZsBio, ZM-0183), mouse-anti-human CD31 (ZsBio, ZM-0044), rabbit-anti-human VIM (Abram, ab92547), mouse-anti-human CD3 (Servicebio, GB12014), mouse anti-human CD4 (ZsBio, ZM-0418), mouse-anti-human CD8 (Servicebio, GB12068), mouse-anti-human CD20 (Servicebio, GB14030), mouse-anti-human CD38 (Servicebio, GB114831), mouse-anti-human CD56 (ZsBio, ZM-0057), rabbit-anti-human CD86 (CST, 91882S), rabbit-anti-human IgA (Abcam, ab124716), rabbit-anti-human PIGR (Abcam, ab96196).

### Tertiary lymphoid structures (TLSs) definition and assessment

We used CD3 and CD20 immunohistochemistry (IHC) to identify tertiary lymphoid structures (TLSs) in our 85 FFPE PSCC tumor sections. CD3 and CD20 are well-established markers for T cells and B cells, which are the primary components of TLS. The use of CD3/CD20 IHC staining is a widely accepted method for the initial identification of TLS based on the presence and spatial organization of T and B cells<sup>32–34</sup>. Only 37 slides contained both tumor and adjacent non-tumor regions within the same tissue section from 85 PSCC cases. To ensure consistency and accuracy in our analysis, our criteria for TLS inclusion: (A) Structured organization: TLS were defined by a clear, organized structure, with B cells and T cells forming distinct zones. (B) Size threshold: only TLS consisting of more than 50 cells were included in the analysis to distinguish them from smaller, less organized immune cell clusters. (C) Normalization by tumor area: the number of TLS was normalized by the area of the tumor sections to provide a consistent measure across samples. This approach aligns with established methods for TLS identification and quantification in tissue sections, which often use similar size thresholds and normalization techniques to ensure robust and reliable data<sup>57,58</sup>.

### IHC Scoring of CD138, IgA, IgG, PIGR and IFN $\gamma$

Specific CD138, IgA, IgG, PIGR and IFN $\gamma$  stained images were analyzed digitally with the image analysis software Image J. The stratification of CD138 expression in our study was based on a semi-quantitative scoring system that combines staining intensity with the percentage of positive cells. The scoring system used was as follows: (0) Negative: No immune cells positive for CD138. (1+) Low: 1–5% of immune cells positive for CD138. (2+) Moderate: 6–20% of immune cells positive for CD138 with moderate or strong intensity, or 6–100% of immune cells with weak intensity. (3+) High: 21–75% of immune cells positive for CD138 with moderate or strong intensity. (4+) Very High: 76–100% of immune cells positive for CD138 with moderate or strong intensity. This scoring system is consistent with those used in previous studies that assessed CD138+ plasma cell density in tissue sections<sup>59,60</sup>. For IgA and IgG, the scoring was based solely on the fraction of positive cells because they are secreted proteins, and the fraction of positive cells is a more direct indicator of the presence of these immunoglobulins in the tissue. The scoring system used was as follows: (0) Negative of immune cells; (1+) 1–5% of immune cells; (2+) 6–20% of immune cells, (3+) 21–75% of immune cells and (4+) 76–100% of immune cells. Similar fraction-based scoring for immunoglobulins has also been applied in studies analyzing immunoglobulin expression in tumor tissues<sup>59</sup>.

For PIGR and IFN $\gamma$  IHC scoring, we measured the integrated optical density (IOD) and area value of the positive signal in each field of view by Image J software, and then calculated the mean density, that is, mean density = IOD/area, which reflects the unit area concentration of the target positive signal. Finally, the average value of the mean density of 5 random areas of each sample was taken as the positive signal intensity value of this sample. The cell staining intensity was scored into 5 levels, (0) Negative: no positive staining, and the positive signal intensity values of the remaining samples were sorted and processed into four categories according to the order ratio of the positive signal intensity values: < 25% was scored as 1 score, 26–50% was scored as 2 score, 50–75% was scored as 3 score, and > 75% was scored as 4 score.

### Flow cytometry

PSCC tumor tissues underwent three to five washes with PBS (1% penicillin-streptomycin, Gibco) were minced into small pieces about 1 to 5 mm<sup>2</sup>, then were digested in 10 mL of 5 mg/mL collagenase type IV (Solarbio C8160-100mg) in Advanced DMEM/F12 (Gibco) containing 2.5% FBS and 1% P/S for 0.5 h at 37 °C gently shaking. Cell

cluster-containing supernatant was collected and centrifuged at  $800 \times g$  for 5 min, and the cell pallet was washed three times using Advanced DMEM/F12.

For single-cell suspensions of tumor samples, flow cytometry was performed by staining with Zombie NIR viability dye (BioLegend, 1:500), blocking with human TruStain FcX™ (BioLegend, 1:100), and staining for 30 min at 4 °C with the following anti-human antibodies: CD45 (BioLegend, HI30, 1:200), CD3 (BioLegend, OKT3, 1:200), CD19 (BD BioLegend, HIB19, 1:200), CD4 (BD Biosciences, RPA-T4, 1:200), CD8 (BD Biosciences, RPA-T8, 1:200). For intracellular cytokine staining of tumor-infiltrating T cells in MC38 tumor samples, cells obtained from the digested tumor mass were incubated in a tissue culture incubator for four hours at 37 °C with Cell Stimulation Cocktail (plus protein transport inhibitors, eBioscience™, 1:500). Surface staining was stained with Zombie NIR viability dye (BioLegend, 1:500), blocked with anti-CD16/32 (BioLegend, 1:100) and analyzed by flow cytometry (Beckman colter, CytoFLEX S) after incubation for 30 min at 4 °C with the following anti-mouse antibodies: CD45.2 (BioLegend, 104, 1:200), CD11b (BioLegend, M1/70, 1:200), TCRβ (BioLegend, H57-597, 1:200), CD8α (BioLegend, 53-6.7, 1:200), GZMB (BioLegend, QA16A02, 1:200), IFN-γ (BioLegend, XMGL2, 1:200) and TNF-α (BioLegend, MP6-XT22, 1:200).

For experiments requiring cell sorting, cells were first incubated with viability factor (Zombie NIR™ Fixable Viability kit) in  $1 \times$  PBS for 15 min, followed by washing with MACS buffer ( $1 \times$  PBS with 0.5% FBS and 2 mM EDTA) and centrifugation at  $800 \times g$  for 5 min and then stained against anti-human CD45 antibody in MACS buffer for 30 min. Cells were then centrifuged again, resuspended in MACS buffer, and sorted using a BD FACSAria™ III cell sorter. Sort cells were collected directly in  $1 \times$  PBS with 0.04% BSA. For Single-cell RNA-seq analysis, live CD45<sup>+</sup> cells from PSCC tumor tissues were sorted by using Fixable Viability Dye Zombie Aqua™ (BioLegend) and anti-human CD45 antibody conjugated to Brilliant Violet 605™ (BioLegend, clone HI30).

### Cell lines and PSCC primary cells

MC38, HT29, Hela and A549 cells were purchased from the American Type Culture Collection. PSCC primary cells was made in our laboratory. All cell lines were proven to be negative for Mycoplasma contamination. All cells were cultured in a 37 °C incubator with 5% CO<sub>2</sub>. All cancer cells, except for PSCC primary cells, were cultured in high sugar DMEM supplemented with 10% FBS and 1% penicillin–streptomycin.

For the establishment and passage of PSCC primary cells, PSCC tumor samples underwent three to five washes with PBS (1% penicillin–streptomycin, Gibco), were minced into small pieces about 1 to 5 mm<sup>2</sup> and then digested in 10 mL of 5 mg/mL collagenase type IV (Solarbio C8160-100 mg) in Advanced DMEM/F12 (Gibco) containing 2.5% FBS and 1% P/S for 0.5 h at 37 °C gently shaking. Then, cell cluster-containing supernatant was collected and centrifuged at  $800 \times g$  for 5 min. Cell pallet was washed three times using Advanced DMEM/F12 and resuspended in PSCC primary tumor cell culture medium (PRSP-ECM-2D, Hefei PreceDo Medical Laboratory Co., Ltd.). Fresh medium was changed every 2 to 3 days. After PSCC primary tumor cell clones were formed, enzymatic digestion was used to remove mixed primary fibroblasts at each cell passage. Repeat the fibroblast removal operation 3–5 times. Finally, cellular immunocytochemistry was used to clarify the type of squamous cell carcinoma (Guangzhou KingMed Diagnostics Group Co., Ltd.). For cell treatment with various cytokines and IgA/IgG, 1 ng/ml IFN-β, 5 ng/ml IFN-γ, 20 ng/ml TNF-α, 10 ng/ml IL-1β, 0.5 μg/ml IgA, and 0.5 μg/ml IgG were used, and the cells were collected 24 hours after stimulation for further RNA isolation. PSCC primary cells, HT29 and Hela cells were also stimulated with 4 ng/ml and 10 ng/ml IFN-γ to quantify PIGR protein level by western blot.

For the generation of stable PIGR expression cell lines in PSCC primary cells and MC38 cells, lentivirus-based plasmids containing human *PIGR* and mouse *PIGR* cDNA were constructed. PSCC primary

cells and MC38 cells were seeded in 24-well plates and infected with hPIGR/mPIGR lentivirus for 72 h, with 8 μg/ml polybrene (Sigma, cat. no. TR-1003). After 72 hours, the infection efficacy was evaluated by ZsGreen fluorescence intensity. DAPI (BioLegend, 422801) was stained for dead cells, and stable PIGR expression cells were sorted by FACS using DAPI-negative and ZsGreen-positive fluorescence for downstream experiments.

### Mice and xenograft tumor models

C57BL/6 wild-type mice (male, 6 weeks old) and BALB/c-Nude mice (male, 6 weeks old) were purchased from GemPharmatech Co., Ltd and Beijing Vital River Laboratory Animal Technology. *IgA*<sup>-/-</sup> mice were purchased from Cyagen Biosciences, and the genetic background was C57BL/6J (male & female, 8 weeks old). All mice were housed in rooms on a standard 12 h light–dark cycle, with a temperature range of 68–72 °F and a humidity range of 30–70%. In all tumor model experiments, 6–12-week-old male mice were used.

For xenograft tumor models,  $5 \times 10^5$  MC38 cells (ctrl- or PIGR-overexpressed) or  $1 \times 10^7$  primary human PSCC cells (wild-type) cells were subcutaneously injected. Tumor volume was calculated as:  $0.5 \times (L \times W^2)$ , in which L is length and W is width. In accordance with the ethical guidelines, subcutaneous tumors were allowed to reach a size not exceeding 10% of the animal's body weight, which constituted the permissible limits established by the ethics board. The maximum permitted tumor burden was not exceeded at any point during the experiment. Tumor tissues were dissected mechanically into single-cell suspensions for flow cytometry or retained for RNA and protein isolation. B cells were depleted from C57BL/6 WT mice by intraocular injection of 200 μg of anti-CD20 antibodies (anti-CD20, BioLegend, SA271G2, Cat#152116, or  $1 \times$  PBS) at the time of tumor cell implantation and again at 10 days intervals to deplete B cells. Mice would be killed if the tumor size/burden exceeded 2.0 cm in diameter. For tumor TME analysis, implanted tumor tissues were removed and digested in 5 mL of 1 mg/mL collagenase type IV (Biosharp, BS165-100mg) in RPMI 1640 containing 40 μg/ml DNaseI (Biosharp, BS137-10mg) for 0.5 h at 37 °C gently shaking. Cell cluster-containing supernatant was collected and centrifuged at  $500 \times g$  for 5 min, and cell pallet was washed three times using MACS buffer for downstream FACS sorting, FCM analysis and other cell assays.

### Western blotting

All cell samples were lysed using the RIPA Lysis Buffer (Beyotime, P0013B) with 1% PMSF. The lysates were separated by 10% SDS-Page and transferred onto PVDF membranes. The membranes were then blocked with 5% milk for 1 h. Following blocking, the membranes were incubated overnight at 4 °C with the primary antibodies: anti-human PIGR (Abcam, ab96196), anti-mouse PIGR (Abclonal, A6130), anti-HA monoclonal antibody (Proteintech, 66006-2-Ig) and anti-beta actin monoclonal antibody (Abcam, ab8226). Then, the membranes were washed with  $1 \times$  TBST and incubated with secondary antibodies at room temperature for 1 h. The protein bands were visualized using the ECL chemiluminescence substrate kit.

### Enzyme-Linked Immunosorbent assays (ELISAs)

IgA/IgG levels in patient plasma/PSCC tumor tissues were determined using IgA/IgG Human SimpleStep ELISA Kit (Abcam, ab196263 & ab195215). IgA/IgG levels in mouse plasma/subcutaneous tumor tissues were determined using IgA/IgG Mouse SimpleStep ELISA Kit (Abcam, ab157717 & ab157719). Follow the product instructions strictly: a. Add 50 μL of all samples or standard to appropriate wells. b. Add 50 μL of the Antibody Cocktail to each well. c. Seal the plate and incubate for 40 min at room temperature on a plate shaker set to 400 rpm. d. Wash each well with Wash Buffer. e. Add 100 μL of TMB Development Solution to each well and incubate for 5 min in the dark on a plate shaker set to 400 rpm. f. Add 100 μL of Stop Solution to each well.

Shake the plate on a plate shaker for 1 min to mix. Record the OD at 450 nm.

### CCK-8 proliferation assays

CCK-8 Cell Proliferation and Cytotoxicity Assay Kit (Solarbio, CA1210) was used to detect cell proliferation. The cells were digested into single-cell suspension, and then the cell suspension was seeded in a 96-well plate (2000 cells/well). Place the culture plate in an incubator to pre-incubate for 8 h (37 °C, 5% CO<sub>2</sub>). Add 10 µl of CCK reagent to each well. Incubate the culture plate in the incubator for 1 h. Use a microplate reader to measure the absorbance at 450 nm. Testing was performed every 24 h until the end of 96 h.

### Colony-formation assays

Cells were cultured in DMEM (10% FBS) for 24 h before seeding and then diluted into a concentration of  $1 \times 10^5$ /ml. A total of 200 cells (2000 of PSCC primary tumor cell) were seeded in 2 ml of DMEM (10% FBS). Treatments were refreshed on day 0 after seeding. On day 12–14, one image was taken per well (three wells per treatment group). Colony number was calculated using ImageJ.

### Transwell migration assays

Cells were starved in FBS-free DMEM for 24 h. Add 600 µl of DMEM containing 20% FBS into the lower chamber of the 24-well plate and use tweezers to place the Transwell chamber into the 24-well plate. The starved cells were digested, resuspended in serum-free DMEM, and 10,000 cells (100 µl) were seeded in the upper chamber. The 24-well plate was cultured at 37 °C and 5% CO<sub>2</sub> for 24 h. Take out the Transwell chamber and gently wipe the cells inside the chamber with a cotton swab. Add 4% paraformaldehyde to fix the cells for 30 min. Add 0.1% crystal violet staining solution and stain for 10 min. Randomly take pictures of 3 fields of view in each chamber and use ImageJ to count and average the number of cells for quantitative research.

### Generation of single-cell RNA-seq libraries and sequencing

For PSCC tumor (P1-P6 and P91-P107) and normal adjacent tissues (P1-P6), whole single cells were centrifuged for 5 min at  $800 \times g$  and were resuspended in PBS with 0.04% BSA. Cells were then counted using the Countess<sup>®</sup> II Automated Cell Counter (Thermo Fisher) with a final viability of > 85%. Single-cell RNA-seq libraries were prepared using the Chromium Single Cell 3' Reagent Kits v3 (10x Genomics). Cell suspensions were loaded onto a Chromium Chip along with the reverse transcription master mix and single-cell gel beads aiming for 2000–10000 single cells per reaction. Following the generation of single-cell gel bead-in-emulsions (GEMs), reverse transcription, purified and amplification were performed. The above single-cell RNA-seq libraries were generated with a unique sample index for each sample and sequenced on an NovaSeq platform (Illumina) to generate 150 bp paired-end reads.

### Alignment, quality control of scRNA-seq data

Following sequencing, Raw data (raw reads) of fastq files were assembled from the raw BCL files using Illumina's bcl2fastq converter and processed through primary quality control. All the downstream analyses were based on the clean data (clean reads) with high quality. Reads from clean data were mapped to the human GRCh38 reference genome by Cell Ranger (10X Genomics, version 6.0.1) pipeline using default parameters to generate gene/barcode matrices.

After alignment using Cell Ranger, a unified gene/barcode matrix for each sample was acquired and read into Seurat (version 4.3.0) for downstream analysis. The 28 single-cell RNA-seq libraries were sequenced to average more than 441 million sequencing reads for each sample, with the average of sequencing saturation (covering the fraction of library complexity) at 63.2%. After creation of the gene/barcode matrices, a cell-level filtering step was performed to remove cells that

expressed fewer than 200 genes, more than 5000 genes and those with more than 10% mitochondrial gene expression. Next, genes that were lowly expressed (genes expressed in fewer than 10 cells) and mitochondrial and ribosomal genes across each sample were removed. Finally, 202,424 single cells from a total of 28 libraries were retained for downstream analysis, with 7138 mean UMIs and of 2209 mean genes per cell.

### Processing and clustering of scRNA-seq data

Gene expression matrices were normalized for library size per cell and log-transformed for better interpretability using the Seurat function 'NormalizeData'. For data integration and batch correction, 'FindIntegrationAnchors' and 'IntegrateData' were applied to the data in Seurat. For previously published HNSCC (GSE103322)<sup>23</sup>, NPC (GSE150430)<sup>24</sup> and cSCC (GSE144236)<sup>25</sup> datasets, files downloaded from GEO Accession Viewer were processed, imported into a Seurat-compatible object and integrated by tumor types for downstream analysis. After generating the library-size normalized and integrated gene/barcode matrix, we next sought to reduce the dimensionality of the data for downstream visualization and clustering. Highly variable genes (top 2000) were identified and selected by 'FindVariableGenes' based on high dispersion and carried forward into scaling and principal component analysis (PCA) using the Seurat function 'ScaleData' and 'RunPCA'. Louvain clustering was performed on all cells with the 'FindClusters' function using the first top PCs and various resolution parameters. And we then used the Seurat function 'RunUMAP' with the equal PCs number for visualization.

### Identification and quantification of cell types in scRNA-seq data

Identification of various cell clusters was performed using the Seurat function 'FindAllMarkers' or 'FindMarkers' in conjunction with the differentially expressed canonical markers. The differentially expressed genes with false-discovery rate (FDR)  $\leq 0.05$  and  $\log_2$ -fold change of average expression  $\geq 0.5$  were considered significantly different in different cell clusters. For integrated data in multi-tumor types, we annotated four major populations in TME according to the classical gene signature. For malignant cells, we used inferCNV (version 1.10.1) to estimate the sample-wise copy number variations (CNVs) following the standard workflow for epithelial cells with default parameters and selected out 9255 malignant cells with high CNVs for further analyses.

We then evaluated the enrichment of cells from a given group type in each cluster by a two-step strategy. Firstly, we summated the cells from total clusters in each sequencing sample, and calculated the proportion of each cluster by dividing sum value of per sample. Secondly, analysis of proportion for sample ratio values by student *t* test was used to determine if the cell enrichment across clusters was statistically significant differences in cell frequencies.

### Bulk B cell receptor sequencing (bulk BCR-seq) and analysis

We collected fresh tumor tissues from 20 PSCC patients (PT11-PT30) and performed bulk BCR-sequencing on the SeqHealth Technology platform to evaluate the types and diversity of immunoglobulin (Ig) isotypes in PSCC. Total RNAs were extracted from cryopreserved snap frozen tumor tissues using TRIzol (Invitrogen<sup>™</sup>, Cat. No. 15596018). About 2 µg total RNA of each sample were used for BCR sequencing library preparation using KC-Digital<sup>™</sup> Stranded BCR-seq Library Prep Kit following the manufacturer's instruction. The library products corresponding to 250–500 bp were enriched, quantified and finally sequenced on the DNBSEQ-T7 sequencer. Library construction failed in 4 cases due to the limited residual tumor tissue, leaving 16 samples (8 HPV<sup>+</sup> and 8 HPV<sup>-</sup>) for downstream analysis.

Following sequencing, clean reads were first assigned to clusters based on identical UMI sequences. Within each cluster, reads were pairwise aligned, and those exhibiting > 95% sequence identity were further extracted into a new subcluster. Once all subclusters were

established, we performed multiple sequence alignment to obtain a consensus sequence for each. These non-redundant consensus sequences served as the input for bulk BCR-seq analysis. Using MiXCR software (version 3.0.3)<sup>61</sup>, the consensus sequences were aligned to the international ImMunoGeneTics (IMGT) database<sup>62</sup> to obtain V, D and J gene fragments, rearrangements and CDR3 sequences. We defined a BCR clone according to the same V(D)J genes, CDR3 nucleotide and amino acid sequences. The diversity of IGH isotype was evaluated by Shannon's entropy, which have been widely used for assessing the diversity of BCR as described<sup>63,64</sup>.

### Survival analysis using The Cancer Genome Atlas

Molecular and clinical data from TCGA for cervical squamous cell carcinoma (CESC), head and neck squamous cell carcinoma (HNSCC) and colon adenocarcinoma (COAD) were downloaded from Genomic Data Commons Xena Hub (<https://gdc.xenahubs.net>). A total of 521 patients with matched clinical information and tumor RNA-seq data was used in this study, including CESC ( $n = 144$ ), HNSCC ( $n = 293$ ), and COAD ( $n = 84$ ). We evaluated the expression of IgA based on the average of *IGHA1* and *IGHA2*. For CESC and HNSCC data, the cutoff of high or low expression for *PIGR* or IgA was the median. For COAD, the lower and upper quartiles of *PIGR* or IgA were selected for clinical grouping. Kaplan–Meier survival analysis and the log-rank tests were performed to compare overall survival between groups.

### PSCC primary cells transcriptome sequencing and analysis

PSCC primary cells in culture in PRS-PECM-2D medium were treated with or without 0.5  $\mu\text{g/ml}$  of natural human IgA or  $1 \times \text{PBS}$  for 24 h. Total RNA was isolated with TRNzol Universal total RNA extraction kits (TIANGEN, DP424). About 2  $\mu\text{g}$  total RNA were used for stranded RNA sequencing library preparation using KC-Digital™ Stranded mRNA Library Prep Kit for Illumina® (Catalog NO. DR08502). The library products corresponding to 200–500 bps were enriched, quantified and finally sequenced on DNBSEQ-T7 sequencer (MGI Tech Co., Ltd. China) with PE150 model.

Following sequencing, raw sequencing data was first filtered by Trimmomatic (version 0.36). Low-quality reads were discarded, and the reads contaminated with adapter sequences were trimmed. Clean reads were further treated with in-house scripts to eliminate duplication bias introduced in library preparation and sequencing. The de-duplicated consensus sequences were mapped to the hg38 reference genome using star (version 2.5.3a) with default settings. Uniquely mapped reads were counted with in-house scripts at the gene-level using GENCODE V38 transcript annotation for human. Principal component analysis was performed with normalized log-transformed data using the R language function 'prcomp'. Differential expression genes analysis was performed using DESeq2 (version.1.34.0)<sup>65</sup>. The significantly expressed genes were selected with foldchange  $\geq 1.5$  and adjusted  $p$ -value  $\leq 0.05$ .

### Signature enrichment analysis

Gene set enrichment analysis (GSEA) was performed by using R package clusterProfiler<sup>66</sup> function 'GSEA' (version 4.0.5) with gene sets (Hallmarks and KEGG) from the Molecular Signatures Database (msigdb, version 7.5.1). Gene Ontology (GO) enrichment analysis in this study was performed by using clusterProfiler or the Metascape online website<sup>67</sup>.

### Statistics & reproducibility

Data are presented as means  $\pm$  SEM. Statistical analyses were performed using GraphPad Prism (v8.4.0) and R (v.4.1.2). A two-tailed paired and unpaired Student  $t$  test between two groups were used to determine significance. Chi-Squared test was used to determine significance for the proportion of high (score  $\geq 3$ ) or low (score  $\leq 2$ ) IHC score between HPV<sup>+</sup> and HPV<sup>-</sup> groups. For time-course analysis of

tumor growth and CCK8 cell proliferation, a two-way ANOVA test was used. Survival was analyzed with the two-sided log-rank (Mantel–Cox) test. Statistical parameters were represented in the Figure Legend of each Figure. Pearson correlation coefficients was computed to evaluate the correlation between two variables.  $P < 0.05$  was considered significant. \* $P < 0.05$ , \*\* $P < 0.01$ , \*\*\* $P < 0.001$ , and \*\*\*\* $P < 0.0001$ . For scRNA-seq data, DEG analysis was performed by using the Wilcoxon rank-sum test. Other statistical analysis used in this paper are described in the corresponding methods. The western blots, HE and fluorescence images shown were selected as representative of results from at least three independent replicate experiments.

### Ethics approval

All human samples, plasma, tumor and adjacent tissues, were collected in accordance with the Declaration of Helsinki. The study design was approved by the Ethics Committee of First Affiliated Hospital of the University of Science and Technology of China. The approval ID is 2016KT67. All animal experimental protocols were approved by the Institutional Animal Care and Use Committee of the University of Science and Technology of China. The approval ID is USTCACUC192401055.

### Reporting summary

Further information on research design is available in the Nature Portfolio Reporting Summary linked to this article.

### Data availability

The raw sequence data generated in this study have been deposited in the Genome Sequence Archive (Genomics, Proteomics & Bioinformatics 2021) in the National Genomics Data Center (Nucleic Acids Res 2022), China National Center for Bioinformation / Beijing Institute of Genomics, Chinese Academy of Sciences that are accessible via <https://ngdc.cncb.ac.cn/gsa-human/browse/HRA008170> (PRJCA024930, scRNA-seq and bulk-BCR-seq for PSCC tissues) and <https://ngdc.cncb.ac.cn/gsa-human/browse/HRA008149> (PRJCA028674, bulk-RNA-seq for primary PSCC cells). Among the 23 tumor samples included in the scRNA-seq dataset, 11 samples (P1–P6 and P91–P95) have already been reported in our previously published work<sup>20</sup>. The raw sequencing datasets PRJCA024930 and PRJCA028674, generated from human tissues, are available under controlled access due to ethical restrictions related to patient privacy. Access can be requested by contacting the corresponding author. Other scRNA-seq data sets used in this study are also publicly available, including HNSCC<sup>23</sup> [<https://www.ncbi.nlm.nih.gov/geo/query/acc.cgi?acc=GSE103322>], NPC<sup>24</sup> [<https://www.ncbi.nlm.nih.gov/geo/query/acc.cgi?acc=GSE150430>] and cSCC<sup>25</sup> [<https://www.ncbi.nlm.nih.gov/geo/query/acc.cgi?acc=GSE144236>]. Source data are provided with this paper. All remaining data are available in the article, supplementary and source data files. Source data are provided in this paper.

### Code availability

All packages used in this study are open-source R packages. DESeq2<sup>65</sup> (version.1.34.0) was used for differential gene expression analyses between bulk RNA-seq samples. ClusterProfiler<sup>66</sup> (version 4.0.5) was implemented for the pathway enrichment work. All scRNA-seq data were analyzed with standard programs and packages, as detailed above.

### References

1. Thomas, A. et al. Penile cancer. *Nat. Rev. Dis. Primers* **7**, 11 (2021).
2. Clark, P. E. et al. Penile cancer: clinical practice guidelines in oncology. *J. Natl. Compr. Canc. Netw.* **11**, 594–615 (2013).
3. Douglawi, A. & Masterson, T. A. Penile cancer epidemiology and risk factors: a contemporary review. *Curr. Opin. Urol.* **29**, 145–149 (2019).

4. Olesen, T. B. et al. Prevalence of human papillomavirus DNA and p16INK4a in penile cancer and penile intraepithelial neoplasia: a systematic review and meta-analysis. *Lancet Oncol.* **20**, 145–158 (2019).
5. Hakenberg, O. W. et al. EAU guidelines on penile cancer: 2014 update. *Eur. Urol.* **67**, 142–150 (2015).
6. Backes, D. M., Kurman, R. J., Pimenta, J. M. & Smith, J. S. Systematic review of human papillomavirus prevalence in invasive penile cancer. *Cancer Causes Control* **20**, 449–457 (2009).
7. Miralles-Guri, C. et al. Human papillomavirus prevalence and type distribution in penile carcinoma. *J. Clin. Pathol.* **62**, 870–878 (2009).
8. Moch, H., Cubilla, A. L., Humphrey, P. A., Reuter, V. E. & Ulbright, T. M. The 2016 WHO classification of tumours of the urinary system and male genital organs-Part A: renal, penile, and testicular tumours. *Eur. Urol.* **70**, 93–105 (2016).
9. Boulet, G., Horvath, C., Vanden Broeck, D., Sahebali, S. & Bogers, J. Human papillomavirus: E6 and E7 oncogenes. *Int. J. Biochem. Cell Biol.* **39**, 2006–2011 (2007).
10. Kayes, O., Ahmed, H. U., Arya, M. & Minhas, S. Molecular and genetic pathways in penile cancer. *Lancet Oncol.* **8**, 420–429 (2007).
11. Sand, F. L., Rasmussen, C. L., Frederiksen, M. H., Andersen, K. K. & Kjaer, S. K. Prognostic significance of HPV and p16 status in men diagnosed with penile cancer: a systematic review and meta-analysis. *Cancer Epidemiol. Biomarkers Prev.* **27**, 1123–1132 (2018).
12. Ottenhof, S. R. et al. The prognostic value of immune factors in the tumor microenvironment of penile squamous cell carcinoma. *Front. Immunol.* **9**, 1253 (2018).
13. Lont, A. P. et al. Presence of high-risk human papillomavirus DNA in penile carcinoma predicts favorable outcome in survival. *Int. J. Cancer* **119**, 1078–1081 (2006).
14. McDaniel, A. S. et al. Genomic profiling of penile squamous cell carcinoma reveals new opportunities for targeted therapy. *Cancer Res.* **75**, 5219–5227 (2015).
15. Wang, Y. et al. Mutational landscape of penile squamous cell carcinoma in a Chinese population. *Int. J. Cancer* **145**, 1280–1289 (2019).
16. Chahoud, J. et al. Whole-exome sequencing in penile squamous cell carcinoma uncovers novel prognostic categorization and drug targets similar to head and neck squamous cell carcinoma. *Clin. Cancer Res.* **27**, 2560–2570 (2021).
17. Cao, J. et al. Correlation between the evolution of somatic alterations during lymphatic metastasis and clinical outcome in penile squamous cell carcinoma. *Front. Oncol.* **11**, 641869 (2021).
18. Kuasne, H. et al. Genome-wide methylation and transcriptome analysis in penile carcinoma: uncovering new molecular markers. *Clin. Epigenet.* **7**, 46 (2015).
19. Elst, L. et al. Single-cell atlas of penile cancer reveals TP53 mutations as a driver of an aggressive phenotype, irrespective of human papillomavirus status, and provides clues for treatment personalization. *Eur. Urol.* **86**, 114–127 (2024).
20. Zhu, L. et al. Single-cell transcriptomic profiling reveals distinct tumor microenvironments in HPV-associated penile squamous cell carcinoma. *Precis. Clin. Med.* **8**, pba013c (2025).
21. Cubilla, A. L. et al. The World Health Organisation 2016 classification of penile carcinomas: a review and update from the International Society of Urological Pathology expert-driven recommendations. *Histopathology* **72**, 893–904 (2018).
22. Stuart, T. et al. Comprehensive integration of single-cell data. *Cell* **177**, 1888–1902 (2019).
23. Puram, S. V. et al. Single-cell transcriptomic analysis of primary and metastatic tumor ecosystems in head and neck cancer. *Cell* **171**, 1611–1624 (2017).
24. Chen, Y. P. et al. Single-cell transcriptomics reveals regulators underlying immune cell diversity and immune subtypes associated with prognosis in nasopharyngeal carcinoma. *Cell Res.* **30**, 1024–1042 (2020).
25. Ji, A. L. et al. Multimodal analysis of composition and spatial architecture in human squamous cell carcinoma. *Cell* **182**, 497–514 e422 (2020).
26. Ruffin, A. T. et al. B cell signatures and tertiary lymphoid structures contribute to outcome in head and neck squamous cell carcinoma. *Nat. Commun.* **12**, 3349 (2021).
27. Cillo, A. R. et al. Immune landscape of viral- and carcinogen-driven head and neck cancer. *Immunity* **52**, 183–199 (2020).
28. Zhang, S. et al. Characteristics of B lymphocyte infiltration in HPV(+) head and neck squamous cell carcinoma. *Cancer Sci.* **112**, 1402–1416 (2021).
29. Hladikova, K. et al. Tumor-infiltrating B cells affect the progression of oropharyngeal squamous cell carcinoma via cell-to-cell interactions with CD8(+) T cells. *J. Immunother. Cancer* **7**, 261 (2019).
30. Pitzalis, C., Jones, G. W., Bombardieri, M. & Jones, S. A. Ectopic lymphoid-like structures in infection, cancer and autoimmunity. *Nat. Rev. Immunol.* **14**, 447–462 (2014).
31. Neyt, K., Perros, F., GeurtsvanKessel, C. H., Hammad, H. & Lambrecht, B. N. Tertiary lymphoid organs in infection and autoimmunity. *Trends Immunol.* **33**, 297–305 (2012).
32. Cabrita, R. et al. Tertiary lymphoid structures improve immunotherapy and survival in melanoma. *Nature* **577**, 561–565 (2020).
33. Helmink, B. A. et al. B cells and tertiary lymphoid structures promote immunotherapy response. *Nature* **577**, 549–555 (2020).
34. Petitprez, F. et al. B cells are associated with survival and immunotherapy response in sarcoma. *Nature* **577**, 556–560 (2020).
35. Sharonov, G. V., Serebrovskaya, E. O., Yuzhakova, D. V., Britanova, O. V. & Chudakov, D. M. B cells, plasma cells and antibody repertoires in the tumour microenvironment. *Nat. Rev. Immunol.* **20**, 294–307 (2020).
36. Wouters, M. C. A. & Nelson, B. H. Prognostic significance of tumor-infiltrating B cells and plasma cells in human cancer. *Clin. Cancer Res.* **24**, 6125–6135 (2018).
37. Patel, A. P. et al. Single-cell RNA-seq highlights intratumoral heterogeneity in primary glioblastoma. *Science* **344**, 1396–1401 (2014).
38. Tirosh, I. et al. Dissecting the multicellular ecosystem of metastatic melanoma by single-cell RNA-seq. *Science* **352**, 189–196 (2016).
39. de Sousa-Pereira, P. & Woof, J. M. IgA: Structure, Function, and Developability. *Antibodies* **8**, 57 (2019).
40. Zhang, Y., Zhang, J., Chen, X. & Yang, Z. Polymeric immunoglobulin receptor (PIGR) exerts oncogenic functions via activating ribosome pathway in hepatocellular carcinoma. *Int. J. Med. Sci.* **18**, 364–371 (2021).
41. Biswas, S. et al. IgA transcytosis and antigen recognition govern ovarian cancer immunity. *Nature* **591**, 464–470 (2021).
42. Ocak, S. et al. Loss of polymeric immunoglobulin receptor expression is associated with lung tumorigenesis. *Eur. Respir. J.* **39**, 1171–1180 (2012).
43. Qi, X., Li, X. & Sun, X. Reduced expression of polymeric immunoglobulin receptor (pIgR) in nasopharyngeal carcinoma and its correlation with prognosis. *Tumour Biol.* **37**, 11099–11104 (2016).
44. Asanprakit, W., Lobo, D. N., Eremin, O. & Bennett, A. J. Expression of polymeric immunoglobulin receptor (PIGR) and the effect of PIGR overexpression on breast cancer cells. *Sci. Rep.* **13**, 16606 (2023).
45. Kaetzel, C. S. The polymeric immunoglobulin receptor: bridging innate and adaptive immune responses at mucosal surfaces. *Immunol. Rev.* **206**, 83–99 (2005).
46. Fristedt, R. et al. Expression and prognostic significance of the polymeric immunoglobulin receptor in esophageal and gastric adenocarcinoma. *J. Transl. Med.* **12**, 83 (2014).
47. Khattar, N. H., Lele, S. M. & Kaetzel, C. S. Down-regulation of the polymeric immunoglobulin receptor in non-small cell lung

- carcinoma: correlation with dysregulated expression of the transcription factors USF and AP2. *J. Biomed. Sci.* **12**, 65–77 (2005).
48. Mandal, G. et al. IgA-Dominated humoral immune responses govern patients' outcome in endometrial cancer. *Cancer Res.* **82**, 859–871 (2022).
49. Wu, Y. et al. Neutrophil profiling illuminates anti-tumor antigen-presenting potency. *Cell* **187**, 1422–1439 (2024).
50. Ager, C. R. et al. KLRG1 marks tumor-infiltrating CD4 T cell subsets associated with tumor progression and immunotherapy response. *J. Immunother. Cancer* **11**, e006782 (2023).
51. Torrejon, D. Y. et al. Antitumor immune responses in B2M-deficient cancers. *Cancer Immunol. Res.* **11**, 1642–1655 (2023).
52. Zhang, B. et al. B cell-derived GABA elicits IL-10(+) macrophages to limit anti-tumour immunity. *Nature* **599**, 471–476 (2021).
53. Biswas, S. et al. Targeting intracellular oncoproteins with dimeric IgA promotes expulsion from the cytoplasm and immune-mediated control of epithelial cancers. *Immunity* **56**, 2570–2583 (2023).
54. Wieland, A. et al. Defining HPV-specific B cell responses in patients with head and neck cancer. *Nature* **597**, 274–278 (2021).
55. Emmanuel, A., Nettleton, J., Watkin, N. & Berney, D. M. The molecular pathogenesis of penile carcinoma-current developments and understanding. *Virchows. Arch.* **475**, 397–405 (2019).
56. Guo, A. N., Yong, L., Tong, L. I. U. & Rong, G. U. O. Comparison between universal primer SPF1/GP6++ and SPF1/GP6+ polymerase chain reaction in detection of various genotypes of human papillomavirus. *Cancer Res. Prev. Treat.* **42**, 882–886 (2015).
57. Vanhersecke, L. et al. Mature tertiary lymphoid structures predict immune checkpoint inhibitor efficacy in solid tumors independently of PD-L1 expression. *Nat. Cancer* **2**, 794–802 (2021).
58. Meylan, M. et al. Tertiary lymphoid structures generate and propagate anti-tumor antibody-producing plasma cells in renal cell cancer. *Immunity* **55**, 527–541 e525 (2022).
59. Lohr, M. et al. The prognostic relevance of tumour-infiltrating plasma cells and immunoglobulin kappa C indicates an important role of the humoral immune response in non-small cell lung cancer. *Cancer Lett.* **333**, 222–228 (2013).
60. Kroeger, D. R., Milne, K. & Nelson, B. H. Tumor-infiltrating plasma cells are associated with tertiary lymphoid structures, cytolytic T-cell responses, and superior prognosis in ovarian cancer. *Clin. Cancer Res.* **22**, 3005–3015 (2016).
61. Bolotin, D. A. et al. MiXCR: software for comprehensive adaptive immunity profiling. *Nat Methods* **12**, 380–381 (2015).
62. Lefranc, M. P. et al. IMGT(R), the international ImMunoGeneTics information system(R) 25 years on. *Nucleic Acids Res.* **43**, D413–D422 (2015).
63. Keylock, C. J. Simpson diversity and the Shannon-Wiener index as special cases of a generalized entropy. *Oikos* **109**, 203–207 (2005).
64. Stewart, J. J. et al. A Shannon entropy analysis of immunoglobulin and T cell receptor. *Mol. Immunol.* **34**, 1067–1082 (1997).
65. Love, M. I., Huber, W. & Anders, S. Moderated estimation of fold change and dispersion for RNA-seq data with DESeq2. *Genome Biol.* **15**, 550 (2014).
66. Wu, T. et al. clusterProfiler 4.0: A universal enrichment tool for interpreting omics data. *Innovation* **2**, 100141 (2021).
67. Zhou, Y. et al. Metascape provides a biologist-oriented resource for the analysis of systems-level datasets. *Nat. Commun.* **10**, 1523 (2019).
- (2023YFC2306203 and 2023YFC2306101), The Strategic Priority Research Program of the CAS (XDB0490000), the CAS Project for Young Scientists in Basic Research (YSBR-074), NSFC grant no. 32170912, and no. 82371828 (to W.P.). Anhui Provincial Key Research and Development Project (202204295107020003 to T.T.), Anhui Provincial Science Fund for Distinguished Young Scholars (2022AH020078 to T.T.), the Key Health Project of Anhui Province (AHWJ2024Aa10158 to T.T.), Major Joint Project of New Medicine of USTC (YD9110002018 to T.T.) and Anhui Provincial Cancer Hospital Project (QLGC 2024003 to T.T.).

## Author contributions

T. Tao designed the research and collected clinical samples. D. Shen collected clinical samples. L. Zhu analyzed sequencing data. L. Zhu and D. Shen conducted the experiments, analyzed the data, wrote the original draft and revised the manuscript. P. Zhang, J. Zhang, and Z. Gu helped with the experiments. D. Cao contributed to relevant discussions. W. Pan and J. Xiao supervised the work. W. Pan designed and funded the research.

## Competing interests

The authors declare no competing interests.

## Additional information

**Supplementary information** The online version contains supplementary material available at <https://doi.org/10.1038/s41467-025-67356-6>.

**Correspondence** and requests for materials should be addressed to Jun Xiao or Wen Pan.

**Peer review information** *Nature Communications* thanks Xin Lu, and the other anonymous reviewer(s) for their contribution to the peer review of this work. A peer review file is available.

**Reprints and permissions information** is available at <http://www.nature.com/reprints>

**Publisher's note** Springer Nature remains neutral with regard to jurisdictional claims in published maps and institutional affiliations.

**Open Access** This article is licensed under a Creative Commons Attribution-NonCommercial-NoDerivatives 4.0 International License, which permits any non-commercial use, sharing, distribution and reproduction in any medium or format, as long as you give appropriate credit to the original author(s) and the source, provide a link to the Creative Commons licence, and indicate if you modified the licensed material. You do not have permission under this licence to share adapted material derived from this article or parts of it. The images or other third party material in this article are included in the article's Creative Commons licence, unless indicated otherwise in a credit line to the material. If material is not included in the article's Creative Commons licence and your intended use is not permitted by statutory regulation or exceeds the permitted use, you will need to obtain permission directly from the copyright holder. To view a copy of this licence, visit <http://creativecommons.org/licenses/by-nc-nd/4.0/>.

© The Author(s) 2025

## Acknowledgements

We thank the animal platform and experiment center for life sciences, USTC. This work was supported by the Key R&D Program of MOST